

2006

## Nonlinear effects in bulk optical materials interacting with femtosecond laser pulses

Paul Conrad Noffke  
*University of Dayton*

Follow this and additional works at: [https://ecommons.udayton.edu/graduate\\_theses](https://ecommons.udayton.edu/graduate_theses)

---

### Recommended Citation

Noffke, Paul Conrad, "Nonlinear effects in bulk optical materials interacting with femtosecond laser pulses" (2006). *Graduate Theses and Dissertations*. 4699.  
[https://ecommons.udayton.edu/graduate\\_theses/4699](https://ecommons.udayton.edu/graduate_theses/4699)

This Thesis is brought to you for free and open access by the Theses and Dissertations at eCommons. It has been accepted for inclusion in Graduate Theses and Dissertations by an authorized administrator of eCommons. For more information, please contact [mschlangen1@udayton.edu](mailto:mschlangen1@udayton.edu), [ecommons@udayton.edu](mailto:ecommons@udayton.edu).

**NONLINEAR EFFECTS IN BULK OPTICAL MATERIALS  
INTERACTING WITH FEMTOSECOND LASER PULSES**

Thesis

Submitted to

The School of Engineering of the

UNIVERSITY OF DAYTON

In Partial Fulfillment of the Requirements for

The Degree

Master of Science in Electro-Optics

By

Paul Conrad Noffke

UNIVERSITY OF DAYTON

Dayton, Ohio

May 2006

## **NONLINEAR EFFECTS IN BULK OPTICAL MATERIALS INTERACTING WITH FEMTOSECOND LASER PULSES**

**APPROVED BY:**



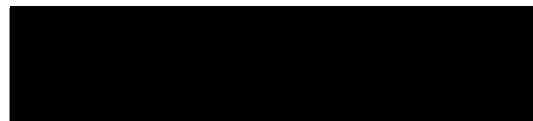
Peter E. Powers, Ph. D.  
Advisory Committee Chairman  
Assistant Professor, Physics  
& Electro-Optics



Christopher D. Brewer, Ph. D.  
Committee Member  
Technical Advisor  
AFRL/MLPJE, WPAFB, OH



Joseph W. Haus, Ph. D.  
Committee Member  
Professor & Director,  
Electro-Optics



Mark A. Walker, Ph. D.  
Committee Member  
Technical Advisor  
AFRL/MLPJE, WPAFB, OH



Donald L. Moon, Ph. D.  
Associate Dean  
School of Engineering



Joseph Saliba, Ph. D., P.E.  
Dean, School of Engineering

## **ABSTRACT**

### **NONLINEAR EFFECTS IN BULK OPTICAL MATERIALS INTERACTING WITH FEMTOSECOND LASER PULSES**

Name: Noffke, Paul C.

University of Dayton, May 2006

Advisor: Dr. Peter E. Powers

The advent of femtosecond lasers has had a major impact on several areas of pure and applied science, especially nonlinear optics. Femtosecond laser pulses not only have the ability to probe material interactions on the femtosecond time scale, but they are also capable of creating peak powers as high as gigawatts from moderate pulse energies available in table-top laser systems. This makes them especially useful tools for studying nonlinear optical phenomena. One spectacular example of such effects is supercontinuum generation. This is a powerful tool in nonlinear optics and has uses in spectroscopy and tunable source development. It can be generated with laser pulses from nanoseconds to femtoseconds, and its detailed origin and behavior in the femtosecond regime is still a subject of active research. Several aspects of this nonlinear effect were examined thoroughly in bulk wide-gap dielectric materials commonly used in optical applications. In addition, several bulk semiconductor materials with optical or infrared applications were tested to determine their nonlinear absorption coefficients. The laser source for the latter experiment was an optical parametric amplifier (OPA) capable of producing femtosecond laser pulses across the wavelength range of 400 to 2400 nm. The OPA was refurbished for this research and to supply a tunable laser source for future work. The overall goal of this research was to examine the nonlinear optical properties of a variety of bulk materials interacting with femtosecond laser pulses.

## TABLE OF CONTENTS

ABSTRACT.....	iii
TABLE OF CONTENTS.....	iv
LIST OF FIGURES .....	vi
LIST OF TABLES .....	ix
CHAPTER 1 – Introduction.....	1
CHAPTER 2 – Optical Parametric Amplifier .....	5
2.1 Theory and Nonlinear Processes.....	6
2.2 Experimental Realization of the OPA.....	17
2.2.1 White-Light Stage .....	18
2.2.2 Pre-Amplification Stage.....	19
2.2.3 Amplification Stage .....	19
2.3 Experimental Setup, Refurbishment and Alignment .....	19
2.4 Characterization .....	24
CHAPTER 3 – Supercontinuum Generation in Bulk Transparent Materials .....	29
3.1 Experimental Setup.....	30
3.2 Supercontinuum Spectra in Bulk Optical Materials .....	34
3.2.1 Crown Glasses .....	35
3.2.2 Ionic Crystals .....	37
3.2.3 Flint Glasses.....	38
3.2.4 Spectral Broadening Summary .....	39
3.3 Conical Emission .....	40
3.4 Supercontinuum Threshold and $f/\#$ Dependence.....	43
3.5 $f/\#$ Spectral Dependence (with Photos).....	47
3.6 Sample Thickness Dependence.....	49
3.7 Backward Emission .....	50
CHAPTER 4 – Supercontinuum Simulations.....	52
4.1 Mechanisms for SCG.....	53
4.2 Modified Nonlinear Schrödinger Equation.....	56
4.3 Supercontinuum Simulations .....	58
CHAPTER 5 – Infrared Material Study at 1550 nm.....	64
5.1 Nonlinear Absorption.....	64

5.2 Experimental Setup and Results .....	67
5.3 Spectral Broadening in IR materials .....	74
CHAPTER 6 – Conclusions.....	75
Appendix A.....	78
REFERENCES .....	83

## LIST OF FIGURES

Figure 2.1 – Vector diagram showing the k-vector relationship to satisfy phase matching.....	8
Figure 2.2 – Type-II phase matching in BBO as a function of phase matching angle.....	11
Figure 2.3 – Phase matching efficiency curves for BBO.....	13
Figure 2.4 – Phase matching acceptance angle for the signal beam at 539 nm and idler beam at 1.55 $\mu\text{m}$ . ....	13
Figure 2.5 – Theoretical bandwidths for the signal and idler at a fixed phase matching angle. ....	14
Figure 2.6 – DFG in the presence of a $\chi^{(2)}$ material showing the generation of the signal and idler beams.....	15
Figure 2.7 – Top-down layout of all the optical elements used in the femtosecond OPA.....	17
Figure 2.8 – White-light continuum generated used to seed the OPA.....	18
Figure 2.9 – Side view of the mixing crystal in the OPA.....	23
Figure 2.10 – OPA signal tuning curve showing signal wavelength versus internal tuning angle.....	25
Figure 2.11 – Maximum signal and idler output energies generated by the OPA.....	26
Figure 2.12 – Spectral measurements of various wavelengths of the signal and idler beams (top). Measured OPA bandwidths plotted versus output wavelength (bottom). ....	27
Figure 3.1 – Experimental setup used to test the supercontinuum properties of various optical windows. ....	31
Figure 3.2 – SCG in quartz generated with a high f/#, (f/52), with an incident peak fluence of 211 $\text{mJ}/\text{cm}^2$ at 775 nm. ....	32
Figure 3.3 – Spectrum of pump and SCG in quartz with focusing conditions at f/35 and 326 $\text{mJ}/\text{cm}^2$ . ....	33

Figure 3.4 – Transmission of the dual notch filter.....	33
Figure 3.5 – SCG spectra of the crown glasses pumped at 775 nm with f/35 and incident laser fluence of 326 mJ/cm <sup>2</sup> .....	36
Figure 3.6 – SCG spectra of the ionic crystals pumped at 775 nm with f/35 and incident laser fluence of 326 mJ/cm <sup>2</sup> .....	37
Figure 3.7 – SCG spectra of the flint glasses pumped at 775 nm with f/35 and incident laser fluence of 326 mJ/cm <sup>2</sup> .....	38
Figure 3.8 – Supercontinuum generation along with conical emission in the crown, ionic, and flint samples .....	41
Figure 3.9 – Center line profile of fused silica continuum seen in Figure 3.8.....	42
Figure 3.10 – Spectra taken to determine the supercontinuum threshold in fused silica. ....	44
Figure 3.11 – SCG threshold data for fused silica using an f/35 lens.....	46
Figure 3.12 – SCG in fused silica.....	48
Figure 3.13 – SCG in CaF <sub>2</sub> .....	48
Figure 3.14 – SCG in SF11.....	49
Figure 3.15 – SCG in three different thicknesses of B270 at 326 mJ/cm <sup>2</sup> using an f/35 system. ....	50
Figure 3.16 – Backwards SCG emission in fused silica (left) and quartz (right). The images have been brightened so the effect can be seen easier.....	51
Figure 4.1 – Plot showing the effects of SPM on a 100 femtosecond laser pulse propagating through fused silica [22]. ....	55
Figure 4.2 – On-axis peak power as the pulse propagates through sapphire.....	59
Figure 4.3 – Final intensity spectrum of the pulse propagated through sapphire. ....	61
Figure 4.4 – Simulated SC spectrum with a 800 nm pump and at 150 fs.....	62
Figure 5.1 – Diagram illustrating the differences between linear and nonlinear absorption.....	65
Figure 5.2 – Nonlinear absorption experiment using the idler output of the OPA.....	69
Figure 5.3 – Diagram illustrating the difference between direct and indirect band- gap semiconductors.....	70
Figure 5.4 – Nonlinear absorption in a 3 mm sample of CdTe.....	71



Figure 5.5 – Nonlinear absorption data in a 1.0 mm InP sample.....	72
Figure 5.6 – Nonlinear absorption in a 5 mm (top) and 0.5 mm (bottom) sample of Si. ....	73

## LIST OF TABLES

Table 3.1 – Summary table of band gaps that were directly measured and previously published values. ....	35
Table 3.2 – Spectral broadening in the bulk windows tested. ....	39
Table 3.3 – Summary table of the observed conical emission angle in the ten samples tested .....	43
Table 3.4 – SCG threshold summary. For the flint glasses 6.52 and 10.4 mJ/cm <sup>2</sup> were the lowest detectable fluence levels for their respective focusing conditions. ....	46
Table 4.1 – Coefficients used in nonlinear SC model. ....	59
Table 5.1 – Theoretical and experimentally measured nonlinear absorption coefficients in three bulk semiconductors.....	74

# CHAPTER 1

## Introduction

Since the invention of the laser in the early 1960s optical science has spawned many new fields of study, and laser applications have become very important in science and technology. Examples of the areas where lasers are making a great impact include the bio-medical and telecommunications industries. Lasers can be classified into two groups: continuous wave or pulsed. Pulsed lasers have evolved considerably since the first mode-locked nanosecond laser built in 1964. Pulses as short as 4.5 femtoseconds at 800 nm have been achieved [1]. In modern commercial laser systems, 100 femtosecond pulses can be created fairly routinely. The time resolution of femtosecond lasers is a clear advantage, but there are other properties that are being exploited. For example, because these laser pulses are so short, extremely high peak intensities can be obtained with modest energies available from a table-top source. Their extremely high intensity can be used for high efficiency nonlinear interactions with applications such as two-photon microscopy and micromachining [2-5]. Femtosecond pulses are also now a new way to probe chemical reactions on a femtosecond time scale [6]. In general, materials exposed to these high peak powers no longer exhibit a linear response to the incident light. Instead they can have a nonlinear response capable of producing spectacular light-matter interactions.

Many science, industrial, and medical fields demand tunable light-sources, and the combination of ultra-short pulses (high peak power) and nonlinear optics has made it possible to cover most desired wavelength ranges. This frequency conversion can also be used to go to even shorter pulse durations by generating excess bandwidth that can then be recompressed. This is accomplished by generating short wavelengths in the ultraviolet or soft x-ray region using focused femtosecond lasers in various gases. The resulting high harmonic generation creates extremely low wavelengths and excess bandwidth that can be recompressed [7]. Traditional frequency conversion in the form of optical parametric amplifiers, pumped with a femtosecond laser, frequency converts the pump into a tunable source capable of producing many different wavelengths depending on the nonlinear crystals used. These different wavelengths are useful for any spectroscopy or pump-probe experiment. In order to utilize the nonlinear optical effects of a material, the properties have to first be measured and well understood.

In this thesis, we will focus on measuring and understanding some of these nonlinear properties by performing experiments on wide band-gap and semiconductor materials using femtosecond lasers. These materials can be utilized for their nonlinear properties in applications context. At high intensities many nonlinear processes take over which cause changes to the pulse as it propagates through the medium. An example of this is supercontinuum generation; one of the most dramatic displays of nonlinear optics and pulse transformation. The input pulse enters a transparent medium at one color, but emerges from the medium as a continuum of colors ranging from the ultra-violet through the visible and into the near infrared. While effect is still not completely understood, many of the mechanisms are known, but a comprehensive explanation of its origin has

yet to be completed, especially for the femtosecond regime. This thesis will examine this nonlinear effect in considerable detail in order to better understand this process.

Chapter 2 begins with a description of the nonlinear optics theory used to explain the nonlinear processes involved in an optical parametric amplifier (OPA). Three main nonlinear effects are explained: second harmonic generation (SHG), difference frequency generation (DFG), and phase matching. Each of these processes is important for understanding the OPA used for subsequent measurements. This chapter also explains how the femtosecond OPA works and the steps taken to refurbish the device to get it back up and running. Finally, the chapter concludes with a detailed characterization of the OPA's signal and idler output beams.

Chapter 3 examines an experimental approach of studying supercontinuum generation. Ten transparent optical substrate materials were tested to determine their white-light properties. Three major categories of glasses were tested including flint, ionic, and crown glasses. The samples were tested under a variety of focusing conditions and excitation energies to explore the effect of supercontinuum generation.

In Chapter 4, a theoretical model of supercontinuum is proposed and tested using a (1+1) dimensional version of the nonlinear Schrödinger equation (NLSE). This model includes all of the nonlinear effects that are currently believed to be important in supercontinuum generation. The model will look at the effects as a function of these terms and is designed to determine which effects contribute to spectral broadening. Currently the model has been applied to only one specific nonlinear medium, because this material has the most complete list of linear and nonlinear properties which are needed as input to the calculations.

Chapter 5 shifts from transparent optical glasses to bulk semiconductor material testing. The nonlinear absorption coefficients of several semiconductor materials were determined using a standard nonlinear absorption experiment. These materials were tested at 1550 nm; primary sources at this wavelength are not readily available on the femtosecond timescale so the OPA was used as the laser source for this experiment. Finally, Chapter 6 provides a summary of the work presented in this thesis and gives final conclusions as well as possible future endeavors.

## CHAPTER 2

### Optical Parametric Amplifier

For many experimental or industrial applications, a tunable source of ultrashort pulses is desirable. Although so-called "tunable" laser sources exist, a given gain medium typically operates over a limited spectral region. For example, dye lasers are often used as tunable ultrashort sources, but each dye has a tuning range of only 5 to 20 nm. These lasers are capable of a tuning range from 320 to 1500 nm, but require working with many different organic dyes which is cumbersome [8]. Other tunable lasers exist such as semiconductor lasers, but they typically have low output energies and poor beam profiles. A solid state laser, Ti:sapphire (Ti:S), is also tunable from 660 to 1180 nm, but this does not cover the whole visible region or any of the telecommunication wavelengths [8]. Through the use of nonlinear optics the spectral region of any one of these lasers can be greatly expanded. This wavelength tunability is accomplished by a device known as optical parametric device (OPD). Through the use of OPDs, 400 to 2500 nm tuning ranges are possible for a device which uses a  $\beta$ -barium borate crystal (BBO). Other nonlinear crystals, such as  $\text{AgGaSe}_2$ , can be used to cover infrared wavelength ranges which extend out to 18  $\mu\text{m}$ , [9]. An OPD is relatively easy to maintain since it uses all solid state materials and over 100 mJ pulse energies are attainable from an OPD [9].

Three types of OPDs will be covered here: an optical parametric amplifier (OPA), an optical parametric generator (OPG), and an optical parametric oscillator (OPO). All

of these devices use nonlinear crystals to convert a pump frequency,  $\omega_p$ , into a signal beam,  $\omega_s$ , an idler beam,  $\omega_i$ , and by most conventions satisfy the following expression,  $\lambda_i > \lambda_s > \lambda_p$ . The OPD used during this thesis was an OPA. The theory and processes will be discussed in detail.

## 2.1 Theory and Nonlinear Processes

To generate a wide spectral range source, there are few nonlinear process such as second-harmonic generation (SHG), white-light continuum generation or supercontinuum generation (SCG), difference frequency generation (DFG) that can be employed. In the case of SHG and DFG, phase matching plays a critical role. For the femtosecond OPA a Ti:S is used as the pump source, SHG is used to generate a new pump beam that drives the OPA. As mentioned above, the signal and idler wavelengths are longer than the pump wavelength. To cover a broader range of wavelengths, SHG shifts the starting pump wavelength to a shorter wavelength. The fundamental Ti:S wavelength allows for tuning starting at 800 nm and covering longer wavelengths. By doubling the Ti:S, we can start at 400 nm to generate wavelengths throughout the visible region (400 to 775 nm) for this OPA. OPAs are typically thought of as a mixing process between two beams. The SHG is the pump, and the second beam, the “seed” pulse this comes from a continuum-generated beam. These beams mix to amplify the seed signal (the continuum) and generate an idler beam by the process of DFG. With the SHG and DFG process, we must phase match the interactions to obtain high conversion efficiency, tunable wavelengths, and conversion over the pulses’ bandwidth. Details about all of these nonlinear processes will be discussed in the following sections.



The basis of nonlinear optics is an induced polarization in the medium that depends on the incident electric field. The polarization  $P$  can be expressed as a power series as shown in the equation below (for a simple scalar case)

$$P = \chi^{(1)}E + \chi^{(2)}E^2 + \chi^{(3)}E^3 + \dots \quad (2.1)$$

The  $\chi^{(n)}$  terms with  $n \geq 2$  are known as nonlinear susceptibilities and  $E$  is the electric field. As mentioned above, the pump for the OPA is obtained using second harmonic generation, which is a second order nonlinear effect dependent on  $\chi^{(2)}$ . A monochromatic laser beam can be represented by the following equation [3],

$$E(t) = E_0 e^{-i\omega t} + c.c., \quad (2.2)$$

where  $E_0$  is the electric field amplitude,  $\omega$  is the carrier frequency, and  $t$  is time. When this field is incident on a nonlinear material with a  $\chi^{(2)}$  susceptibility, there is an induced nonlinear polarization from Equation (2.1) which results in the following [10], where only the terms at  $2\omega$  are considered,

$$P^{(2)}(t) = 2\chi^{(2)}EE^* + (\chi^{(2)}E^2 e^{-2i\omega t} + c.c.). \quad (2.3)$$

From this nonlinear polarization there is a contribution of a frequency at  $2\omega$ , or SHG.

In the OPA, there are four laser beams present at different locations: the fundamental, pump, signal and the idler beam. The fundamental beam comes from a Clark-MRX Ti:S laser at 775 nm. This beam is used to create the white-light continuum, and it is also frequency doubled to act as the pump beam. The signal beam resulting from continuum generation is generated in the visible between 390 and 775 nm, and the idler is generated in the infrared between 775 and 2400 nm. In order to conserve energy, the following equation must be satisfied,

$$\omega_p = \omega_s + \omega_i, \quad (2.4)$$

where  $\omega_p$  is the pump frequency,  $\omega_s$  is the signal frequency, and  $\omega_i$  is the idler frequency.

For Equation (2.4) to satisfy the phase matching condition the following must also be true [10]

$$\Delta k = k_s + k_i - k_p, \quad (2.5)$$

where  $k_s$  is the signal wave number,  $k_i$  is the idler wave number, and  $k_p$  is the pump wave number. Figure 2.1 shows the relationship from Equation 2.5 in a vector diagram that satisfies phase matching.

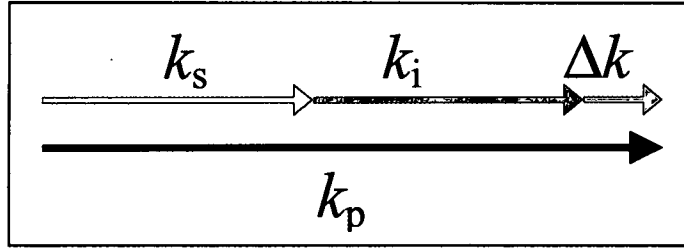


**Figure 2.1 – Vector diagram showing the k-vector relationship to satisfy phase matching.**

In the case of perfect phase matching  $\Delta k = 0$ . The phase matching efficiency drops off rapidly when  $\Delta k$  does not equal zero. The expression for the efficiency is,

$$I = I_0 \text{sinc}^2(\Delta k l / 2), \quad (2.6)$$

where  $I$  is the intensity,  $I_0$  is the peak intensity,  $l$  is the crystal length and the function “sinc” is defined as  $\sin(x)/x$ . From this equation, the theoretical phase matching angle and bandwidth can be determined. If perfect phase matching is assumed, Equation (2.5) can be written in a more useful way

$$\omega_p n_p = \omega_s n_s + \omega_i n_i. \quad (2.7)$$

In order to satisfy phase matching, a birefringent crystal such as BBO can be used. BBO is a negative uniaxial crystal, i.e. two of its principal refractive indices are equal and greater than the third. The common convention for labeling the indices in a nonlinear crystal is  $n_x = n_y = n_o$ , and  $n_z = n_e$ . There is one polarization direction for which  $n_o$  equals  $n_e$ . This is known as the optic axis. In this type of crystal a general incoming polarization can be decomposed in to a component normal to the optic axis (the ordinary ray) which sees  $n_o$  and a component that is not perpendicular (known as the extraordinary ray) which sees  $n_e$ . The extraordinary index  $n_e(\theta)$  depends on the angle of propagation ( $\theta$ ) with respect to the optic axis, in the following way,

$$n_e(\theta) = \sqrt{\frac{1}{\frac{\sin^2 \theta}{n_e^2} + \frac{\cos^2 \theta}{n_o^2}}} \quad (2.8)$$

The indices  $n_e$  and  $n_o$  are the principal indices of the material, where  $\theta = 90^\circ$  for  $n_e$  and  $\theta = 0^\circ$  for  $n_o$  [10]. By using a combination of pump, signal, and idler polarizations, it is possible to rotate the crystal to satisfy Equation (2.7). A specific angle will be phase matched for a specific pair of signal and idler wavelengths. By rotating the crystal, these wavelengths can then be tuned.

BBO is a negative uniaxial ( $n_o > n_e$ ) crystal. A nonlinear crystal is cut in a specific way such that proper phase matching can be achieved in the wavelength region desired. The crystal cut angle is the angle between the optical axis and the entrance normal to the surface. The BBO crystal in the OPA was cut at  $33^\circ$  in this experiment.

In order to change the wavelength of the OPA the crystal angle is tuned. This can be accomplished due the continuum seed. All the wavelengths are present in the white-light continuum, so small changes in the index of refraction from rotations of the BBO

crystal result in different phase matching conditions that generate different signal and idler wavelengths. Two types of phase matching can occur, type-I exists when the polarizations of the signal and idler are the same. Type-II phase matching occurs when they have opposite polarizations. In the OPA, type-II phase matching is used because it allows for easier separation of the signal and idler beams since they have different polarizations. Type-II is also used because higher conversion efficiencies can be obtained and there is more control of the amplified bandwidth for pulse compression. However, in type-I phase matching there is a higher effective nonlinearity, so higher pump intensities are needed to obtain the same amount of gain in type II as type I [11, 12]. The equation that governs this phase matching is [10]

$$n_p^e \omega_p = n_s^e \omega_s + n_i^o \omega_i. \quad (2.9)$$

By substituting  $\omega = 2\pi c / \lambda$  into Equation (2.9), it can be rewritten in a more convenient form to predict the wavelengths that can exist under type-II phase matching

$$\frac{n_p}{\lambda_p} = \frac{n_s}{\lambda_s} + \frac{n_i}{\lambda_i}. \quad (2.10)$$

Equations (2.8) and (2.10) can be used to generate a plot of the allowed signal and idler wavelengths versus the crystal phase matching angle. The plot for type-II phase matching for a 391 nm pump wavelength is shown in Figure 2.2. A 391 nm pump wavelength is used so that the signal beam will cover the visible spectral range and the idler will cover the near infrared. If the OPA was pumped with 800 nm the signal would cover the near infrared and the idler range would extend further out into the infrared.

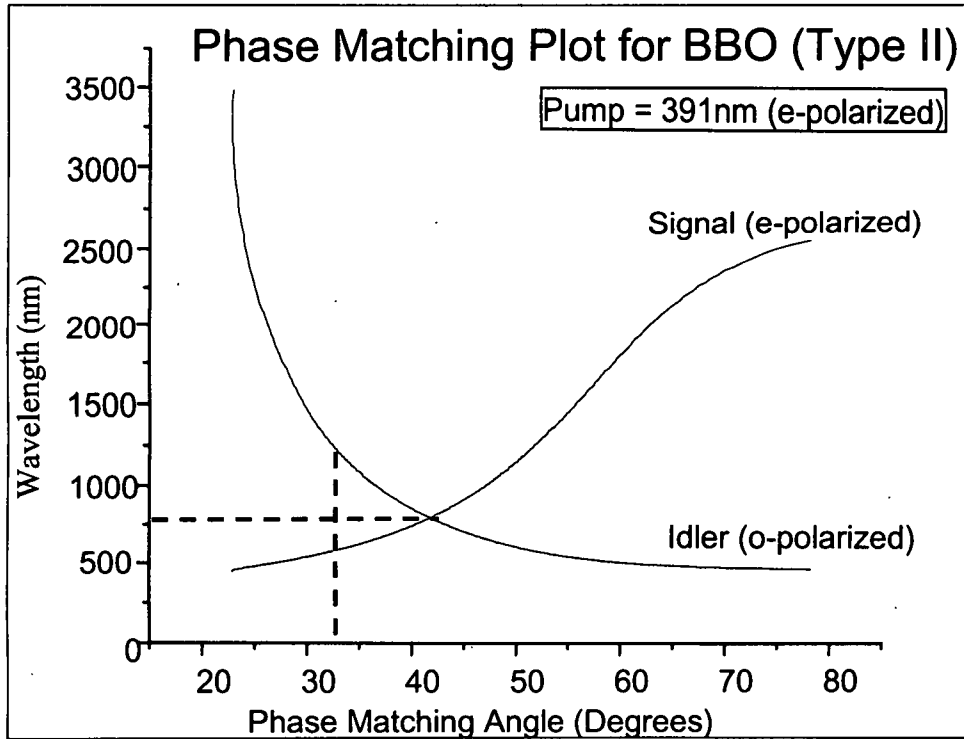


Figure 2.2 – Type-II phase matching in BBO as a function of phase matching angle.

The indexes of refraction used for BBO were determined by the Sellmeier equations shown below [13]

$$\begin{aligned} n_o^2 &= 2.7471 + \frac{0.01878}{\lambda^2 - 0.01822} - 0.01354 \cdot \lambda^2 \\ n_e^2 &= 2.3174 + \frac{0.01224}{\lambda^2 - 0.01667} - 0.01516 \cdot \lambda^2 \end{aligned} \quad (2.11)$$

From the above plot, it can be seen why the crystal was cut at 33°. This cut angle ensures symmetric tuning around normal incidence to the crystal such that the OPA signal can be tuned between 450 to 700 nm.

In Figure 2.2 perfect phase matching is assumed. From Equations (2.5) and (2.6) the phase matching bandwidths and acceptance angle dependences can be calculated. The expression for  $\Delta k$  for can be written as

$$\Delta k = \frac{2\pi n_p(\theta)}{\lambda_p} - \frac{2\pi n_o}{\lambda_s} - \frac{2\pi n_e}{\lambda_i}, \quad (2.12)$$

where  $n_p(\theta)$  is defined by Equation (2.8),  $n_o$  and  $n_e$  are the ordinary and extraordinary indices of refraction for the nonlinear crystal, and  $\lambda_p$ ,  $\lambda_s$ , and  $\lambda_i$  are the corresponding pump, signal, and idler wavelengths respectively. The use of the Sellmeier equations from Equation (2.11) will give a complete expression for  $\Delta k$ . To predict the acceptance angle and bandwidth Equation (2.6) must be used, and it is shown below in its full form,

$$I = I_0 \text{Sa}^2 \left( \left( \frac{2\pi \sqrt{\frac{1}{\frac{\sin^2 \theta}{n_e^2} + \frac{\cos^2 \theta}{n_o^2}}}}{\lambda_p} - \frac{2\pi n_o}{\lambda_s} - \frac{2\pi n_e}{\lambda_i} \right) \frac{l}{2} \right). \quad (2.13)$$

This is a function of three variables  $\theta$ ,  $\lambda_s$ , and  $\lambda_i$ . The others,  $\lambda_p$ ,  $n_e$ , and  $n_o$ , are all fixed parameters. Using Equation (2.4),  $\lambda_i$  can be written in terms of  $\lambda_s$  and Equation (2.13) becomes an equation of two variables. This can then be plotted in three dimensions. Figure 2.3 shows a contour plot of Equation 2.13 using the material properties for the BBO crystal and the pump wavelength.

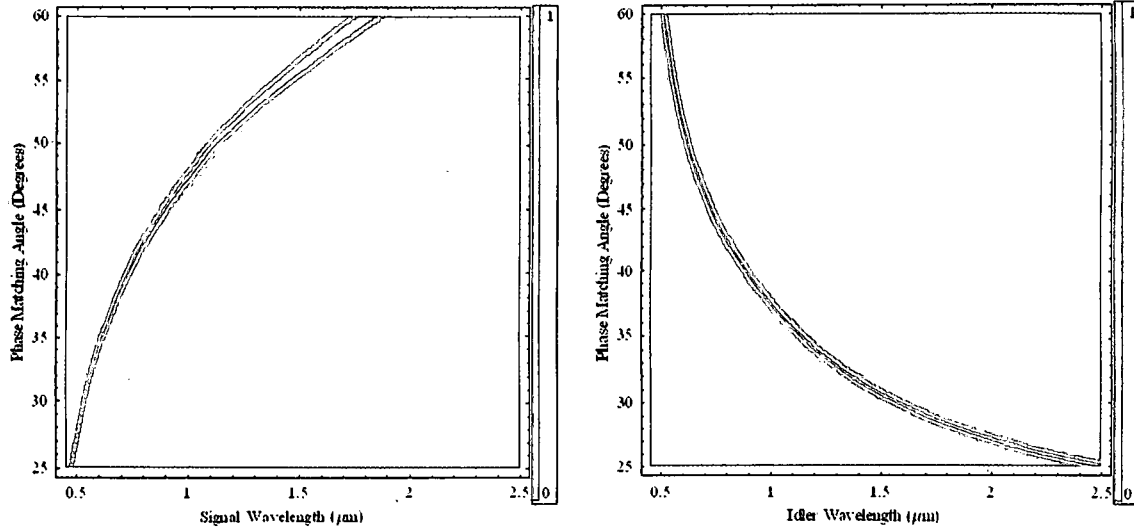


**Figure 2.3 – Phase matching efficiency curves for BBO from these curves the theoretical bandwidths and acceptance angles can be determined, left plot, (a), is the phase matching condition for the signal beam, right plot, (b), for the idler beam.**

The crystal length used in the calculations was 3 mm since this is the length of the BBO crystal in our OPA. In order to find the acceptance angle to achieve phase matching, the line profile of any phase matching angle from above can be taken. This angle dependence has a sign-over-argument behavior, and at its maximum,  $\Delta k$  equals zero.

Figure 2.4 shows the line profile taken from plots (a) and (b) from Figure 2.3.

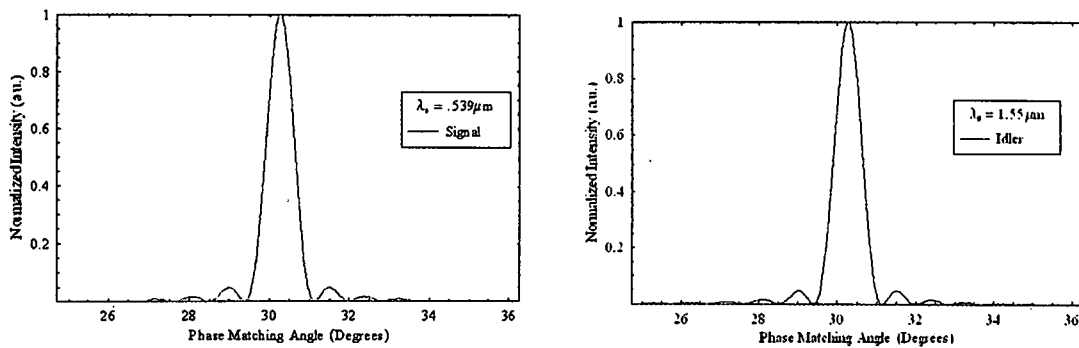


**Figure 2.4 – Phase matching acceptance angle for the signal beam at 539 nm (from Figure 2.3a) and idler beam at 1.55  $\mu\text{m}$  (from Figure 2.3b).**

Likewise, the theoretical bandwidth can be determined by taking a line profile of the Figure 2.3 anywhere along the wavelength axis. Figure 2.5 shows the bandwidths of

both the signal and the idler. The idler bandwidth is considerably larger in terms of wavelength than the signal, but in terms of an energy bandwidth it is the same as the signal. As the phase matching angle is increased, both the signal and idler beams increase in wavelength and bandwidth based on this theory. For a femtosecond OPA, the bandwidth of the process must be large enough to support the femtosecond bandwidth for optimum conversion. The bandwidths shown here are actually the lower limit since the pump is broad-band.

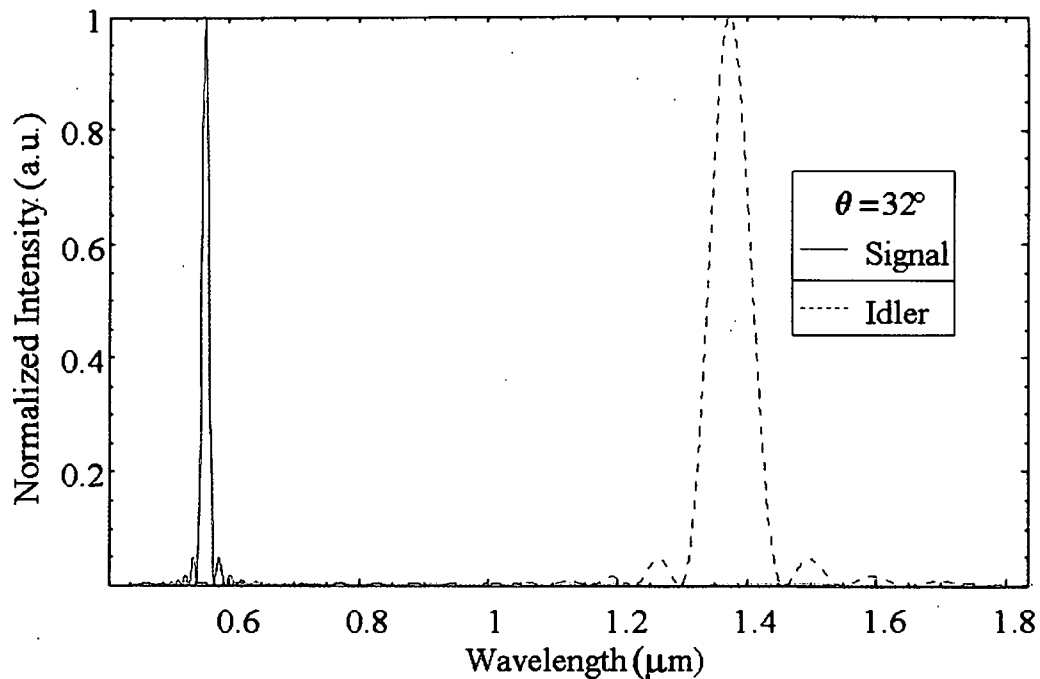


**Figure 2.5 – Theoretical bandwidths for the signal and idler at a fixed phase matching angle.**

Now that the phase matching conditions are understood and satisfied, the nonlinear processes that make an OPA work can be introduced. The OPA is the same as difference frequency generation (DFG) since a DFG process between a pump and signal generates an idler and amplifies the signal. This is a direct consequence of energy



conservation: for every idler photon generated, a signal photon is also generated and a pump photon used up. This is shown in Figure 2.6. In the OPA that was put together for this thesis experiment, the process starts with a fixed input (the SHG of the Ti:S) and a weak seed (white-light continuum) in a  $\chi^{(2)}$  material to stimulate the creation of a third frequency (the idler). Once  $\omega_i$  exists, it stimulates the creation of even more  $\omega_s$  photons, leading to the exponential growth of both the signal and the idler [9]. The virtual level diagram shown in Figure 2.6 also shows how the signal and idler beam are generated due to difference frequency generation.

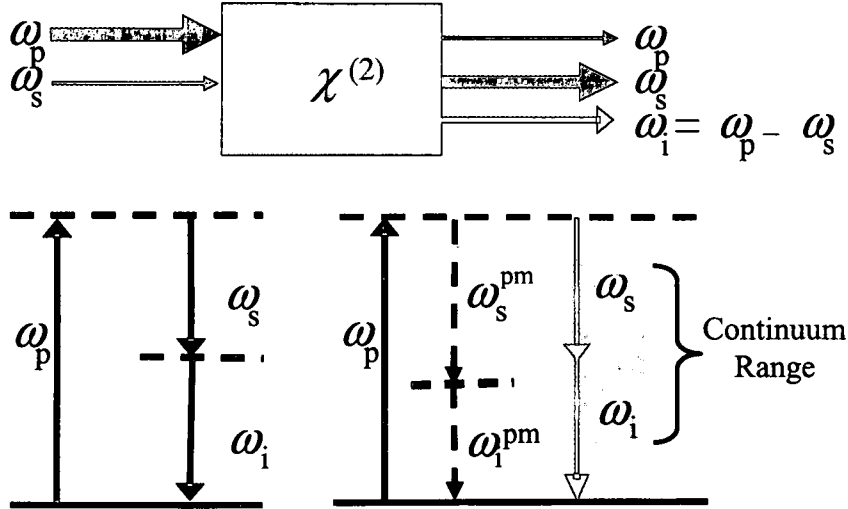


Figure 2.6 – DFG in the presence of a  $\chi^{(2)}$  material showing the generation of the signal and idler beams. Virtual levels show the stimulation of the signal and idler due to the continuum seed. The gray box shows the various range of possibilities for a phase matched signal  $\omega_s^{pm}$  and idler  $\omega_i^{pm}$ .

The coupled amplitude equations for DFG are:

$$\frac{dA_s}{dz} = \frac{8\pi\omega_s^2 d_{eff}}{k_s c^2} A_p A_i^* e^{i\Delta k z}, \quad (2.13)$$

$$\frac{dA_i}{dz} = \frac{8\pi\omega_i^2 d_{eff}}{k_i c^2} A_p A_s^* e^{i\Delta k z}, \quad (2.14)$$

where  $A_s$ ,  $A_i$ , and  $A_p$  are the amplitudes for the signal, idler, and pump respectively, and  $d_{eff}$  is the effective nonlinearity. The solution for Equations (2.13) and (2.14) under the condition of an undepleted pump and where  $A_i(0) = 0$ , leads to the solution shown below [10],

$$A_s(z) = A_s(0) \cosh(\kappa z), \quad (2.15)$$

$$A_i(z) = i \left( \frac{n_0 \omega_i}{n_e \omega_s} \right)^{1/2} \frac{A_p}{|A_p|} A_s^*(0) \sinh(\kappa z), \quad (2.16)$$

where  $\kappa$  is defined by the following,

$$\kappa^2 = \frac{32\pi^2 \chi^{(2)} \omega_s^2 \omega_i^2}{k_s k_i c^4} |A_p|^2. \quad (2.16)$$

In Equation (2.16),  $\chi^{(2)}$  is the second order nonlinear susceptibility. Essentially the signal and idler amplitudes grow as a function of  $z$  and the OPA amplifies the signal and idler outputs. This process is known as parametric amplification, and it makes an OPA such a unique and powerful device.

## 2.2 Experimental Realization of the OPA

The OPA used in these experiments can be broken up into three different stages as shown in Figure 2.7

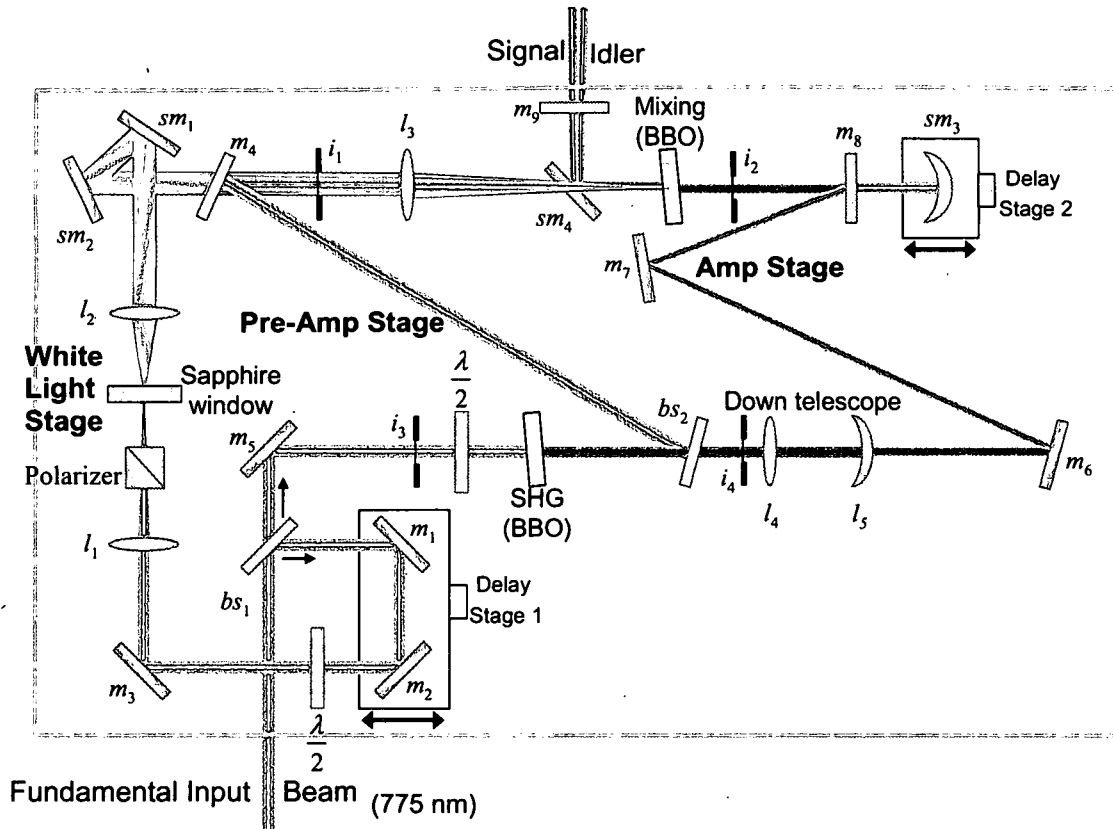
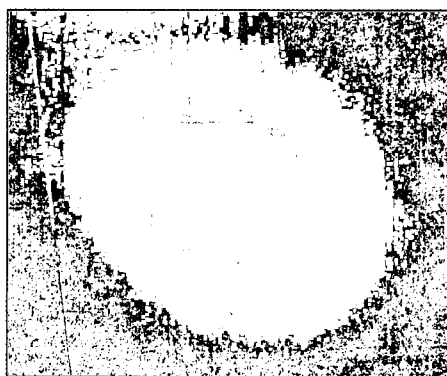


Figure 2.7 – Top-down layout of all the optical elements used in the femtosecond OPA.

The first stage is the white-light continuum stage. This stage “seeds” the OPA by providing a weak signal to stimulate DFG in the nonlinear crystal. The second stage is the pre-amplification stage. In this stage, the seed and a portion of the pump subtract to form a difference frequency and to generate a specific amplified signal and weak idler beam. The final stage is the amplification stage. In this stage the parametric amplification occurs which boosts the signal and idler beams to appreciable energies.

### 2.2.1 White-Light Stage

The white-light continuum is a powerful effect in nonlinear optics. This effect is still not completely understood, but many of the mechanisms and properties are known. In later sections, the white-light continuum will be studied rigorously for a variety of materials. For now, it can be considered as a broadband emission with a spectral range covering 400 to 1100 nm. The visible part of the continuum is used to seed the OPA. The continuum is generated by using a 50 mm focal length lens and focusing approximately 1  $\mu$ J of the fundamental beam (775 nm) into a window made of sapphire. The optimum white-light should appear on a screen with a white lobe in the center (the continuum) surrounded by a red ring. This red ring is known as conical emission and will be discussed in greater detail later. A half-wave plate/polarizer combination is used to adjust the energy incident on the sapphire window to optimize the continuum for better OPA performance. The red ring portion it is used as a reference because this continuum seed generates highest output power for the signal and idler beams. A digital photo of this continuum can be seen in Figure 2.8.



**Figure 2.8 – White-light continuum generated used to seed the OPA.**

### **2.2.2 Pre-Amplification Stage**

In this stage a small portion of the pump beam (~10%) is mixed with the white-light continuum in the nonlinear BBO crystal. When proper phase matching has been achieved within the crystal, DFG occurs and a weak signal beam and idler beam are created. This process takes place in the first pass through the crystal, but this is not where the amplification occurs. In this OPA, the upper half of the nonlinear crystal is used to generate the signal and idler. The next stage uses the lower half for parametric amplification.

### **2.2.3 Amplification Stage**

In the final stage, the remaining portion of the pump beam is used to amplify the signal and idler beams. This beam is combined with the newly generated signal and idler beams from the pre-amplification stage in the lower half of the BBO crystal. This is where the nonlinear process of parametric amplification occurs and amplifies the signal and idler beam. This is the second pass through the BBO crystal making efficient use of the nonlinear medium. The experimental setup of this system requires many optical components and very sensitive alignment, but once operational, this OPD provides any wavelength desired in the visible or near infrared. These are the tunable laser emissions from the OPA that are used in experimental research

## **2.3 Experimental Setup, Refurbishment and Alignment**

The OPA used for this research was a Clark Vis-OPA<sup>TM</sup>. This is a standard commercial device using all of the above theory. The experimental lay-out of this device

can be seen in Figure 2.7. This device however, had damaged optics, mis-aligned telescopes, and the nonlinear crystals used were old and degraded. The first step in getting this OPA operating correctly again was re-aligning the telescopes and mirrors so that damage would not occur in any optical component. The components of this optical system were examined as well as elements replaced. We took precautions to avoid damage within the system. All of the lenses used in this system were of unknown focal length. The focal lengths ( $f$ ) were measured using the simple thin lens approximation,

$$\frac{1}{f} = \frac{1}{s_o} + \frac{1}{s_i}, \quad (2.15)$$

where  $s_o$  is the object position and  $s_i$  is the image position. Just after entering the OPA, the fundamental beam is split sending a portion of it to the white-light stage using  $bs_1$ . Less than 2  $\mu$ J are sent to this stage. The first three mirrors are dielectric stacks designed to be 99.9% reflective around 775 nm. The half-wave plate polarizer combination used was an attenuator to control the continuum. The first lens,  $l_1$ , in the white light stage is used to focus the light into the sapphire window to generate the white-light continuum to seed the OPA, and its focal length is 100 mm. The second lens,  $l_2$ , is used to collimate the continuum that will be used in the pre-amplification stage; its focal length is 50 mm. The mirrors used to steer the white-light into the next stage are silver mirrors which are commonly used as broadband mirrors. They are ~95% reflective through the visible and into the near IR. In this stage, there is no real threat of damage to any components because only ~1  $\mu$ J of energy is being used.

One of the split Ti:S fundamental beams from  $bs_1$  is used for the continuum generation and the other is doubled in a BBO crystal. The doubling is enabled by using the remaining fundamental beam from  $bs_1$  and directing it through the half-wave plate.

This plate is used to control the polarization and allows for the best possible phase matching of the fundamental beam going into the BBO crystal where second harmonic generation occurs. The resulting output at 390 nm is used as the pump in the rest of the OPA.

In the pre-amplification stage, a portion of the SHG-pump beam is split off using  $bs_2$  sending approximately 10% to be mixed with the white-light in the BBO mixing crystal. The mirror,  $m_4$ , is a dielectric stack which is 99% reflective for wavelengths only around 390 nm, and it allows all other wavelengths to pass. The lens used in the pre-amplification stage,  $l_3$ , is used to focus the collinear white-light continuum and the pre-amplification beam (which is a roughly 10% of the pump) directly into the nonlinear crystal. Its focal length is 125 mm. Normally focusing into an optical element can cause damage, but in this stage the pulse energies are well below the damage threshold for a BBO crystal. The damage threshold reported in BBO at 390 nm and 150 fs was 300 GW/cm<sup>2</sup> [14]. Mis-alignment in the amplification stage however, can cause serious damage to many elements in the OPA.

To align the pre-amplification stage the continuum and the pre-amplification pump beam should be aligned through the two irises  $i_1$  and  $i_2$ . Since a pulsed laser is being used, the pulses from the continuum and the pre-amplification beam have to be temporally aligned. This is done by using delay stage 1. When the beams are aligned through the irises and temporally overlapped, a flash of light generated by DFG in the mixing crystal should be seen after the crystal as the delay is swept thru through the overlap point. If the crystal is normal to the incoming light the flash will be green.

In the amplification stage, the first set of lenses  $l_4$  and  $l_5$  are used to reduce the spot size of the pump beam. If these lenses are not spaced properly, damage can occur in the OPA. The focal lengths of these two lenses are 200 and -75 mm respectively, and they are arranged to act as a Galilean telescope. The equation to determine the angular magnification factor  $M$  in this telescope is  $M = -f_4/f_5$ , where  $f_4$  is the focal length of  $l_4$  and  $f_5$  is the focal length of  $l_5$ . The angular magnification for this telescope is 2.67. The Galilean telescope is used as a down collimator reducing the input beam diameter by a factor of 2.67. When the lenses are placed a distance of the sum of their focal lengths, a collimated input beam exits the telescope as a reduced collimated beam [15]. The input spot size ( $1/e^2$  diameter) was 5.7 mm and the down collimated spot size was 2.2 mm. Any misalignment of this telescope can result in damage to several elements in the OPA. The pump beam is the only beam with high enough intensity to cause damage in an optical element. The mirror,  $m_8$ , was damaged several times in the early operations/use of the OPA refurbishment due to improper spacing of lenses  $l_4$  and  $l_5$ . Other mirrors that are also vulnerable to damage in this stage are  $m_6$ ,  $m_7$ ,  $m_8$ ,  $sm_4$ ,  $m_9$ , and the BBO mixing crystal. Damaging the nonlinear crystal would be a costly mistake. In the amplification stage, alignment is critical. While Figure 2.8 is a top view the OPA. Figure 2.9 shows a side view of the BBO mixing crystal.



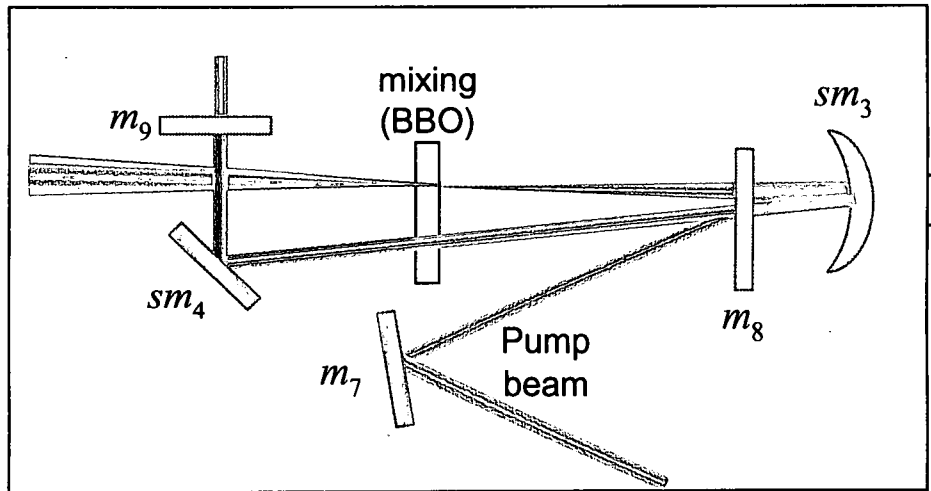


Figure 2.9 – Side view of the mixing crystal in the OPA.

From Figure 2.9, the pre-amplification takes place in the upper portion of the crystal and the amplification takes place in lower half. The mirror,  $sm_3$ , is a gold concave mirror used to re-collimate the newly created signal and idler beams and redirect them through the mixing crystal in co-alignment with the pump beam to achieve parametric amplification. Mirrors,  $m_7$  and  $m_8$ , are dielectric mirrors designed only to reflect light around 390 nm into the mixing crystal. The mirror after the mixing crystal,  $sm_4$ , is the pick off mirror. It is positioned below the incoming continuum and pre-amplification beams but at a height to catch the amplified signal and idler beams in order to direct them out of the OPA. The final element in the OPA,  $m_9$ , acts like a notch filter and does not allow the residual pump beam out of the OPA. Caution must be taken when aligning the pump beam for parametric amplification, if this beam passes over  $sm_4$  it can be focused onto  $m_4$  from  $l_3$ . In this stage damage can occur very easily to many different optical elements in the system, so caution must be used anytime the OPA needs to be realigned.

To begin the alignment in the amplification stage the pump beam needs to be aligned through irises  $i_3$  and  $i_4$ . Next,  $m_7$  and  $m_8$  are adjusted to co-align the pump beam

with the signal and idler for parametric amplification. The pump pulse has to be temporally aligned with both the signal and idler pulses. This is done using delay stage 2. If the beams are co-aligned and temporally overlapped, a bright beam should be seen in the visible depending at what angle the BBO mixing is tuned. For the best signal output and ease in alignment the mixing crystal should be normal to any incoming beam. This allows for the most efficient phase matching. Once the OPA is roughly aligned so there is reasonable conversion of the signal and idler, the only mirrors that need to be adjusted day-to-day are  $m_4$  and  $m_8$ . Small adjustments in these two mirrors and the delay stages are the best way to optimize the OPA each day. The SHG BBO crystal is mounted so it can be rotated in plane normal and perpendicular the fundamental beam. Small changes in these angles improve the phase matching and should also be tweaked day-to-day to optimize the OPA.

## 2.4 Characterization

The OPA characterization includes tuning angle, output energy, bandwidth, and M-squared values for both the signal and idler beams. The tuning angle versus signal wavelength was completed first; this tells us what wavelengths can be converted by the OPA and where they are converted relative to the crystal tuning angle. The signal and idler beam's wavelength was measured using a fiber coupled Ocean Optics spectrometer. As the BBO mixing crystal was rotated the corresponding crystal angle was measured versus wavelength. The tuning angle was read from the mount the mixing crystal was in. The curve was then fit with the type II phase matching curve that relates to the BBO crystal. This plot can be seen in Figure 2.10. The computer program SNLO was used to generate

this fit along with the type I phase matching curve shown for comparison [16]. Due to the index of refraction of the BBO crystal there was a slight offset of the actual measured signal to the theoretical phase matching curve. This occurs due to Snell's laws as the beam pass through the medium. The measured offset was  $0.7^\circ$  and has been corrected for in Figure 2.10. Originally it was unknown whether type I or type II phase matching was occurring in the crystal, from the plot below it became quite clear once the two phase matching curves were plotted. Also we verified that the polarizations were that of the type II interaction.

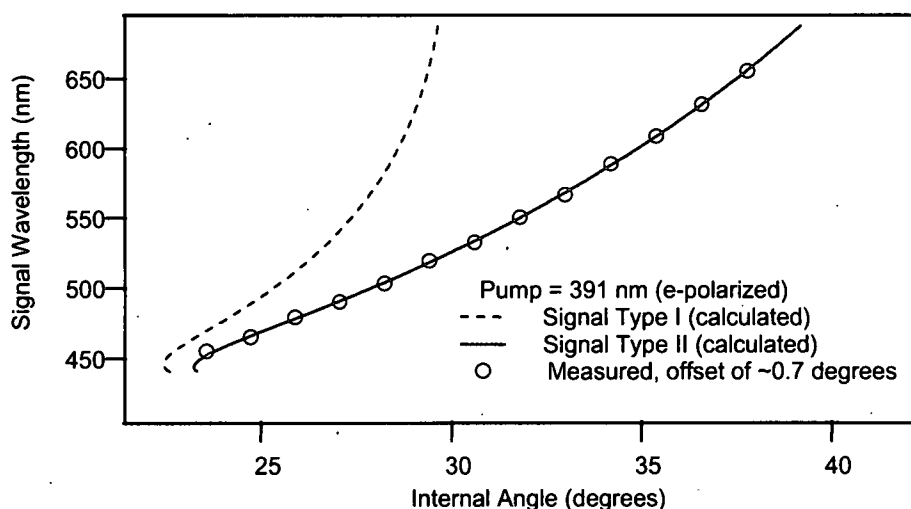


**Figure 2.10 – OPA signal tuning curve showing signal wavelength versus internal tuning angle. The internal angle is the angle of the rotation stage where the BBO is mounted.**

The output energy was measured for various wavelengths for both the signal and idler beams with a pyroelectric joulemeter (Molelectron J3-09) that has a flat response from 0.2 to 10  $\mu\text{m}$ . The signal was measured directly out of the OPA without any filters. The signal and idler beam do not exit the OPA collinear, so there is not a risk of measuring both at the same time. When the crystal is normal to all incoming beams, the

best phase matching is achieved. At the angle of normal incidence the OPA converts the fundamental beam (775 nm) into approximately 530 nm light for the signal and 1500 nm for the idler. This is convenient because 532 nm is a popular laser frequency used in the visible and 1550 nm is a telecommunication wavelength commonly used. Figure 2.11 shows the output energies for the signal and idler beams as a function of wavelength. From the figures, it can be seen as the crystal is tuned away from 530 nm the output energies decrease because the phase matching efficiency is reduced.

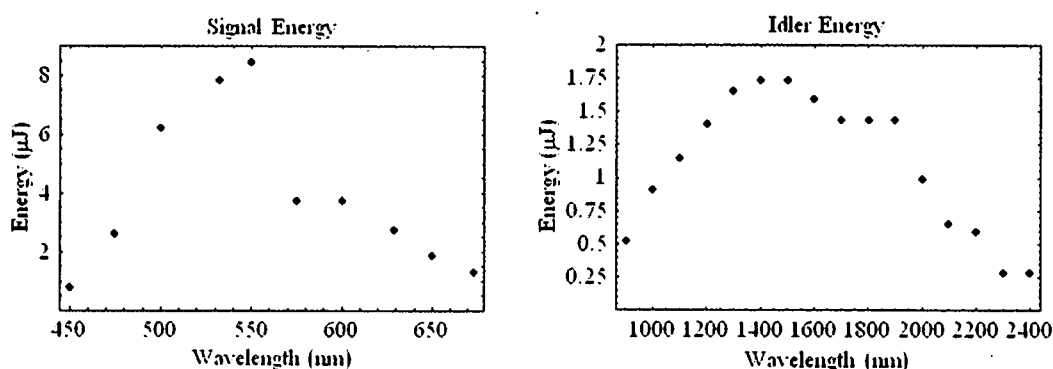


**Figure 2.11 – Maximum signal and idler output energies generated by the OPA.**

The bandwidths of the OPA output were measured spectrally using a fiber coupled Ocean Optics spectrometer. The bandwidth of the signal beam remained constant as the wavelength was changed. For the idler beam the bandwidth increased as wavelength increased which is in agreement with the theory presented previously. The spectra of the various signal and idler emissions can be seen in Figure 2.12 as well as their measured bandwidths.

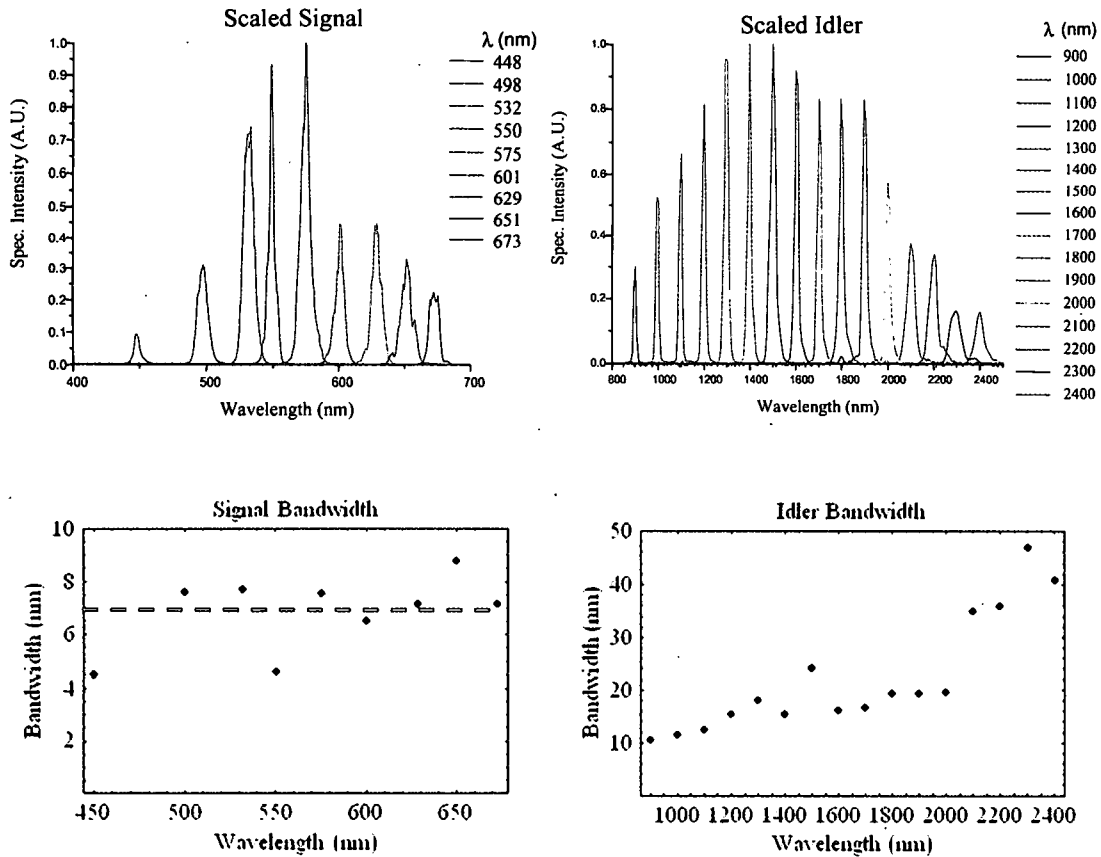


**Figure 2.12 – Spectral measurements of various wavelengths of the signal and idler beams (top). Measured OPA bandwidths plotted versus output wavelength (bottom). The red, dashed line is the bandwidth of the fundamental beam.**

The  $M^2$  values for the output beams of the OPA are fairly consistent with the fundamental input beam. The  $M^2$  is the measure of how fast a Gaussian beam will diverge compared to an ideal (i.e. diffraction limited) Gaussian beam. An ideal Gaussian beam has an  $M^2$  value of one. If the beam is not ideal it will diverge faster and have a larger beam waist than would be predicted by classical Gaussian beam equations. This value is determined by measuring the spot sizes of a laser at different positions through focus. At least four Rayleigh ranges should be covered when measuring the spot sizes

through the focused beam. To determine the M-squared value the spot sizes and positions are fit to the following equation [8],

$$\omega^2(z) = \omega_0^2 + M^4 \left( \frac{\lambda^2}{\pi^2 \omega_0^2} \right) (z - z_0)^2, \quad (2.16)$$

where  $\omega_0$  is the beam waist,  $M^2$  is the dimensionless beam parameter,  $\lambda$  is the wavelength of the laser,  $z_0$  is the position at focus, and  $z$  is the distance from  $z_0$ . Any change in alignment within the OPA can have a fairly significant effect on the output beams M-squared values. Typical  $M^2$  values for the signal and idler beams are around 1.5. Sometimes the  $M^2$  values increased above 2, but then there was usually an alignment issue where the beam may be partially clipping an optical elements edge. Clipping in the BBO mixing crystal is fairly common since the crystal aperture is only 7 mm.

## CHAPTER 3

### Supercontinuum Generation in Bulk Transparent Materials

When intense, ultrashort laser pulses are focused into a transparent optical material significant spectral broadening can be observed. This broadening is known as supercontinuum generation (SCG) or white-light generation and can occur in many different media such as wide band gap transparent solids, liquids and gases [17-19]. The supercontinuum (SC) spectrum is capable of covering the entire visible and near infrared range, making this a valuable spectroscopic tool. This chapter will focus on the experimental study of various bulk, optical windows including flint, ionic, and crown samples. The properties that will be determined include: spectral broadening, conical emission divergence, continuum threshold,  $f/\#$  dependence, and sample thickness dependence.

SCG has been an active area of research over the last five decades, and yet there is still an incomplete understanding of this nonlinear process. Alfano and Shapiro were the first to observe SCG by focusing picosecond pulses into glass [20]. The first continuum produced was with 530 nm pulses and its spectrum covered 400 to 700 nm. Now spectral broadening has been observed, from femtosecond (fs) pulses at 1.5  $\mu\text{m}$ , extending from 400 to 1750 nm [21]. The first theories of the origin of SCG included self-phase modulation (SPM), ionization, and four-wave mixing. Today, self-focusing is consistently regarded as a major mechanism in SCG. Self-focusing depends on the Kerr

nonlinearity ( $n_2$ ), and occurs when a high power laser propagates through a Kerr medium. The critical power,  $P_{crit}$  above which catastrophic self-focusing of a source beam,  $\lambda_0$  occurs is defined as (for a continuous wave laser beam) [23],

$$P_{crit} = \frac{3.77\lambda_0}{8\pi n_0 n_2}. \quad (3.1)$$

It has been shown that the critical power coincides with onset of SCG in many materials [19, 24]. It has also been shown that larger band gap materials tend to have large blue broadening while smaller band gap materials exhibit less [25]. This trend will be seen clearly in the following sections.

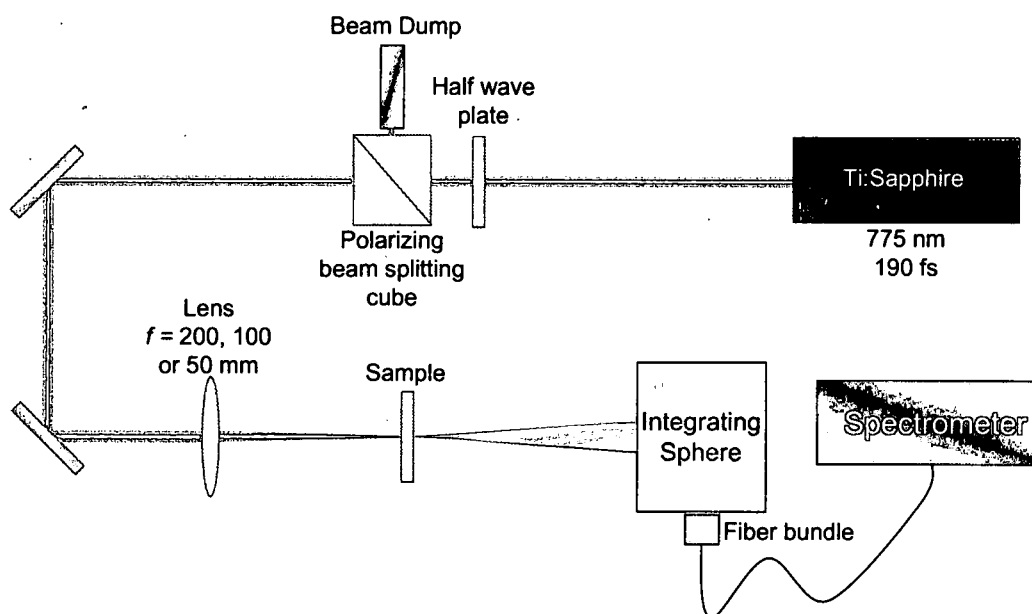
### 3.1 Experimental Setup

The continuum study was preformed using a pump wavelength of 775 nm from a Clark CPA 2010 Ti:sapphire laser system. This laser system has near TEM<sub>00</sub> transverse modes, with typical  $M^2$  values less than 1.5, and produces laser pulses around 150 fs. In the white-light experiment performed, the beam spot size going into the experiment was 5.77 mm ( $1/e^2$  diameter) with an average  $M^2$  value of 1.5 and an average pulse width of 155 fs. In this experiment, three different  $f/\#$  systems were used to generate continua, an  $f/35$ ,  $f/18$ , and  $f/9$ . The continua was then gathered with a collecting lens and focused into an Ocean Optics FOIS-1 fiber optic integrating sphere so the broadband light was sampled evenly and all emission angles collected. The FOIS-1 has a Spectralon integrating sphere with a 99% reflectivity from 400 to 1750 nm [22]. The mixed output of the sphere was coupled into a fused silica fiber bundle with a flat the transmission curve from 250 to 1100 nm, but with a 10% dip in transmission at 950 nm. The fiber bundle was integrated to a Labview® driven ISA SPEX 270M spectrograph used with a



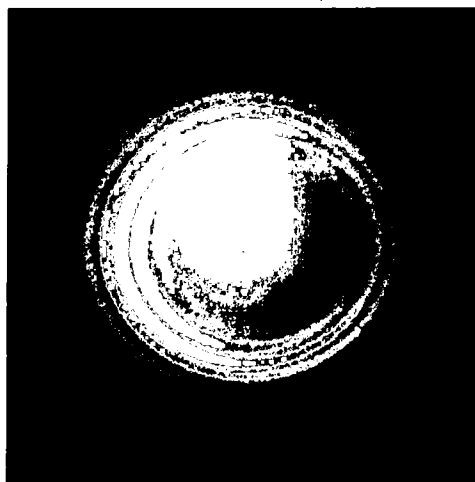
Princeton Instruments, PIXIS 16-bit CDD camera. The CCD was thermo-electrically cooled to  $-70^{\circ}\text{C}$  to improve the signal to noise ratio. This spectrometer has a spectral range from 380 to 1080 nm using a 500 grooves/nm grating.

Figure 3.1 shows the experimental schematic used to generate and collect continua. The half waveplate/beam splitting cube combination was used as a variable attenuator. This setup was used to spectrally determine the dependences of broadening, divergence, threshold,  $f/\#$ , and sample thickness. Note: when the lens is changed the sample position is adjusted such that the focus is in the center of the sample.



**Figure 3.1 – Experimental setup used to test the supercontinuum properties of various optical windows.**

Digital photos of the generated continua projected on a white screen were taken to see the qualitative differences between each sample. A typical continuum picture exhibiting conical emission in quartz is shown in Figure 3.2.



**Figure 3.2 – SCG in quartz generated with a high f/#, (f/52), with an incident peak fluence of  $211 \text{ mJ/cm}^2$  at 775 nm. The photograph was taken with a Sony DSC-F717 camera after 12 cm of propagation in air.**

The explanation of conical emission will be explained in a later section. The broadband emission can be seen in the white center lobe of Figure 3.2. The spectral properties of SCG can be used in many optical applications. A typical continuum spectrum can be seen in Figure 3.3. (The two lines around 810 and 835 nm in the pump spectrum are due to Raman effects in the fused silica fiber used to couple the light into the spectrometer.) This is a characteristic spectrum from a wide band gap transparent material; it has an asymmetric shape with significant blue broadening. A dual notch filter, with lines at 775 and 390 nm was placed between the sample and the detector to increase the effective dynamic range of the spectrometer. Without this filter, the pump beam dominates the collected signal and the blue and red ends of the continuum spectra are lost in the noise of

the spectrometer when the fundamental is just under the saturation limit. The transmission curve of the dual notch filter can be seen in Figure 3.4.

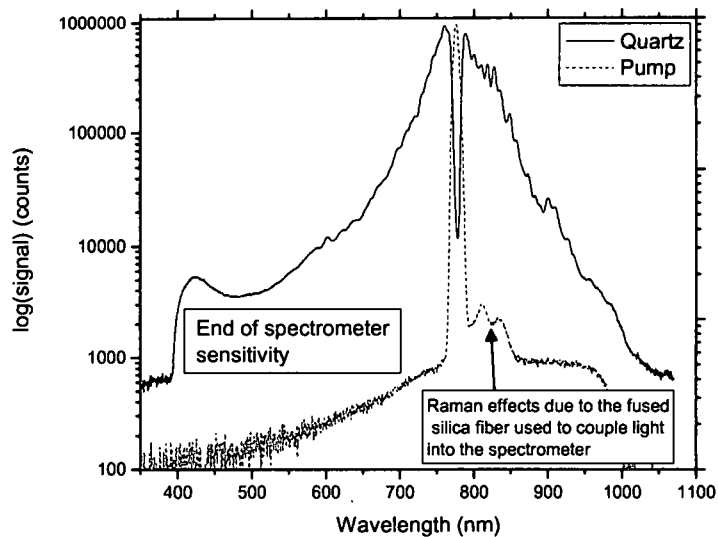


**Figure 3.3 – Spectrum of pump and SCG in quartz with focusing conditions at  $f/35$  and  $326 \text{ mJ/cm}^2$ .**

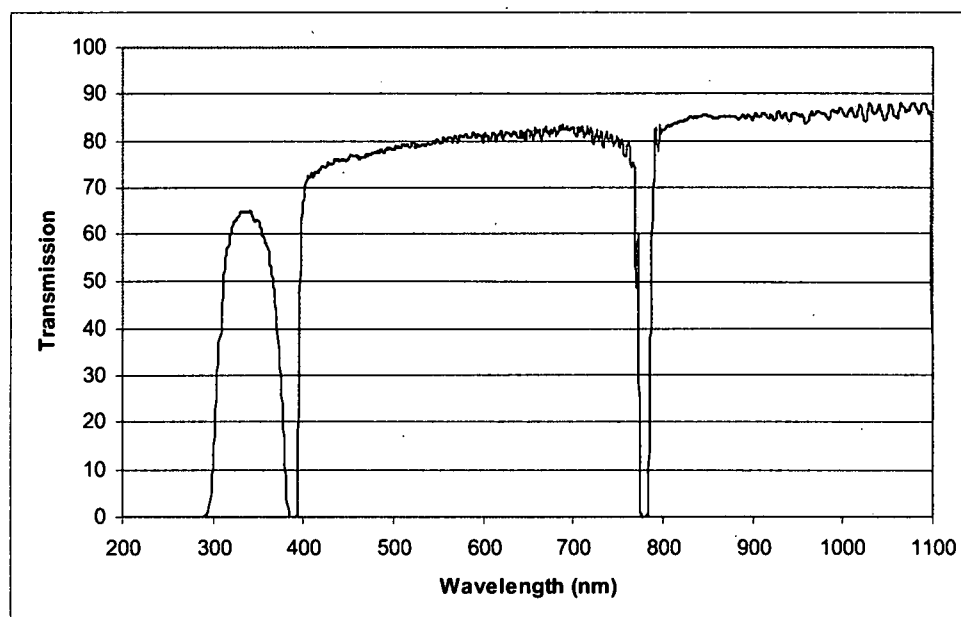


**Figure 3.4 – Transmission of the dual notch filter used to notch out the fundamental pump beam so the wings of supercontinuum spectra could be resolved.**

### 3.2 Supercontinuum Spectra in Bulk Optical Materials

The spectral properties of SCG are of interest because of their spectroscopic and optical usefulness. Ten optical transparent materials were studied in this experiment and can be broken down into three categories: flint and crown glasses and ionic crystals. Four of the samples are classified as crown glasses and they include BK7, fused silica, B270, and SK11. Four other samples are in the ionic crystal group and they are  $\text{CaF}_2$ ,  $\text{KCl}$ ,  $\text{MgF}_2$ , and quartz. The final two samples tested were flint glasses which included SF5 and SF11. Spectra were taken for each sample to determine the spectral properties produced under various focusing conditions. The spectral width of SCG will also exhibit a material band-gap dependence, materials with highest band gap having largest spectral broadening [18]. Table 3.1 is a summary of the materials which were tested during this experiment and their band-gaps. Previous experimental work has shown an approximately linear dependence of blue broadening on band-gap [18]. Some of the materials did not have documented band-gaps so they were measured experimentally by measuring where the transmission cutoffs off in the ultra-violet. This cutoff can be related to the material band-gap by the following relation [8],

$$E_g = \frac{h\nu}{e} = \frac{1239 \text{ nm} \cdot \text{eV}}{\lambda_c}. \quad (3.2)$$

The cutoff wavelength was measured using a Cary-500 UV-Vis spectrometer which was capable of measuring transmission from 185 to 3000 nm.

**Table 3.1 – Summary table of band gaps that were directly measured and previously published values.**

Material	Cutoff $\lambda$ (nm)	$E_g^a$ (eV)	$E_g^b$ (eV)	Ref.
SF5	319	3.9		
SF11	362	3.4	3.3	[25]
B270	280	4.4		
BK7	264	4.7		
Fused Silica	<185		7.5	[25]
SK11	266	4.7		
CaF <sub>2</sub>	<185		10.2	[23]
KCl	<185		8.7	[27]
MgF <sub>2</sub>	<185		11.3	[28]
Quartz	<185		9.2	[29]
<sup>a</sup> Experimentally measured linear transmittance UV cutoff				
<sup>b</sup> Documented band gap				

### 3.2.1 Crown Glasses

From the data, the crown glasses were found to be efficient continuum generators. Figure 3.5 shows the emitted spectra for each of the crown glasses tested. The spectra are plotted on a log scale versus photon energy since this more closely related to the physics than the wavelength. The pump spectrum is also included in the plot. The sharp cutoff in the spectrum of fused silica at 400 nm is from the notch filter at 390 nm and is also near the end of the spectrometer spectral range. The band gaps of fused silica is the highest among the crown glasses, at 7.5 eV [25], whereas BK7, B270, and SK11 all have band gaps around 4.5 eV and have similar cutoffs on the blue end of their spectrum. From Figure 3.5, the experimental data indicates that the highest band gap material exhibits the strongest blue broadening. This is the same trend that was observed by Brodeur and Chin in Ref. 25. Spectral broadening on the red side is fairly uniform and does not exhibit any

material dependence due to the supercontinuum mechanisms which will be described in Chapter 4.

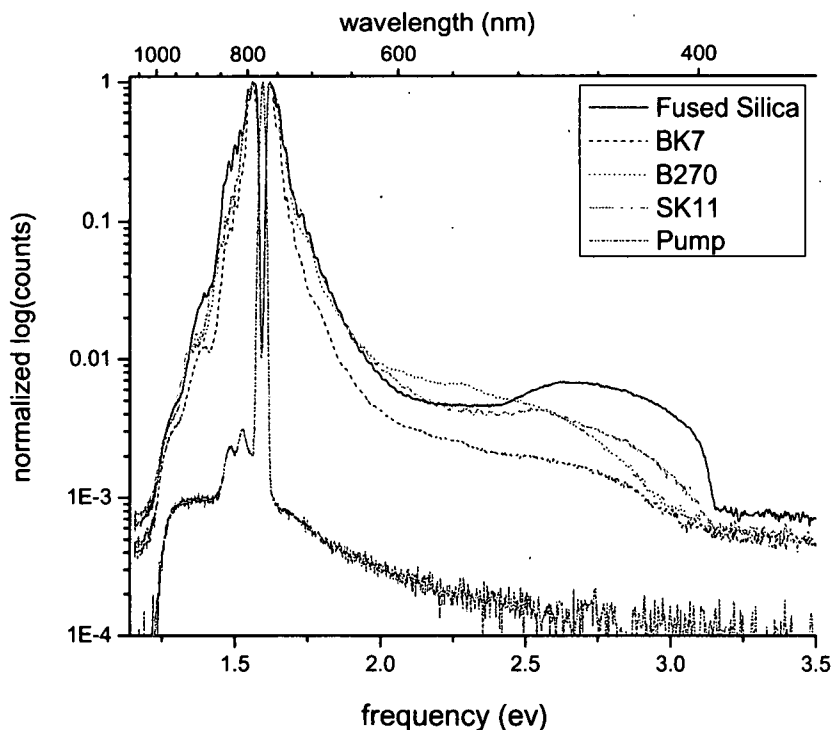


**Figure 3.5 – SCG spectra of the crown glasses pumped at 775 nm with f/35 and incident laser fluence of 326 mJ/cm<sup>2</sup>. A notch filter used to block out the pump to increase S/N.**

Another feature of these spectra to note is the peak in the fused silica spectrum around 2.75 eV (or 450 nm). Such emission has been previously observed in a sapphire window and has been attributed to conical third-harmonic emission [26]. This mechanism uses the  $(2n + 1)$ -order nonlinearity to produce a frequency shift towards the end of the blue broadened spectrum. Also this process is phase matched without birefringence allowing it to occur in all centrosymmetric materials.

### 3.2.2 Ionic Crystals

The ionic crystals demonstrate the strongest SC among our samples tested. They all have blue pedestals that extend beyond 400 nm, making them the best converters of white light due to their large band gaps. Figure 3.6 shows the spectra of the ionic crystals. These large band-gap materials behave consistently with the trend that large band-gap materials exhibit blue pedestals extending out into the ultraviolet [18]. Also, KCl having the smallest band gap has the lowest amount of blue broadening.

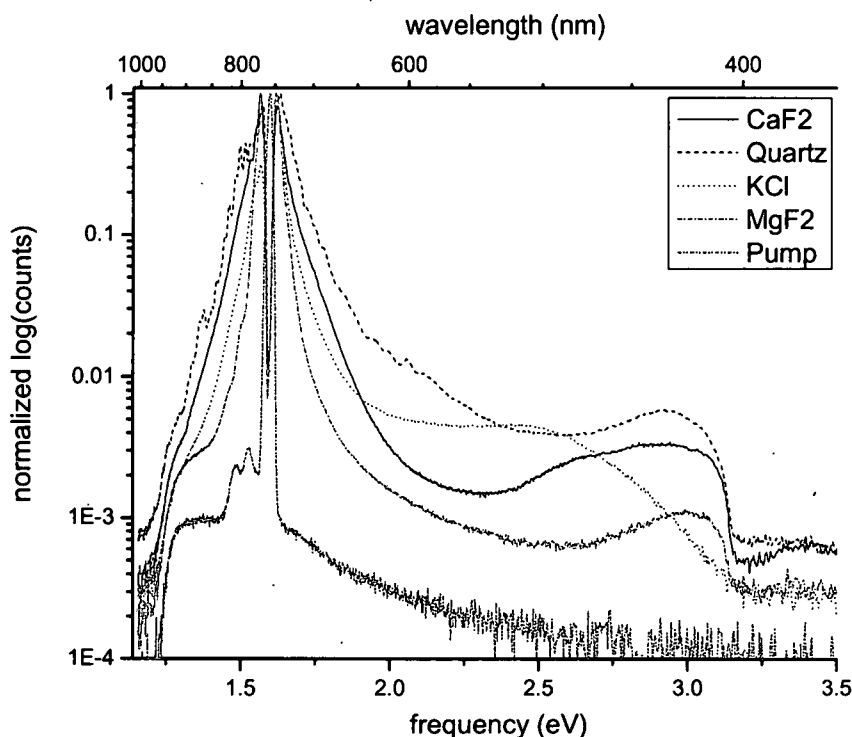


**Figure 3.6 – SCG spectra of the ionic crystals pumped at 775 nm with  $f/35$  and incident laser fluence of  $326 \text{ mJ/cm}^2$ . A notch filter used to block out the pump to increase S/N.**

The ionic crystals, except for KCl, extend past the limits of the spectrometer. Also, with the exception of KCl the other three materials exhibit conical third harmonic emission

under these focusing conditions. The noise floors are at different heights in some of the spectra because of different integration times used for the CCD camera and slight changes in the background emissions.

### 3.2.3 Flint Glasses

Figure 3.7 shows the spectral properties of the flint glasses.

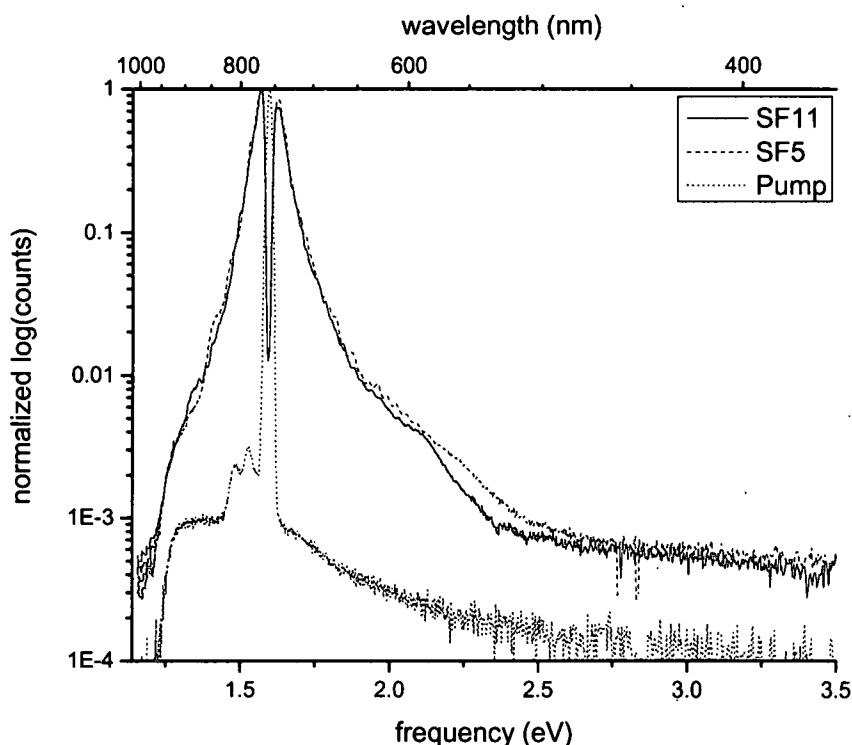


Figure 3.7 – SCG spectra of the flint glasses pumped at 775 nm with f/35 and incident laser fluence of  $326 \text{ mJ/cm}^2$ . A notch filter used to block out the pump to increase S/N.

Since these glasses have the smallest band-gap, they are significantly worse white light generators compared to the other glasses tested. Here the broadening is symmetric about the pump beam and does not show a characteristic blue pedestal. It has been shown that



materials with such small band-gaps do not exhibit the blue pedestal. The incident photon energy needs to be four times larger than the materials band-gap to have the characteristic blue broadening [18].

### 3.2.4 Spectral Broadening Summary

The spectral properties are one of the most important properties in SCG because of its use in spectroscopy, tunable laser sources, and optical pulse compression. A summary of spectral broadening shown in Figures 3.4-6 can be seen in Table 3.2. The cutoffs were determined by measuring the wavelengths just above the noise floor. The spectral range of the spectrometer was 380 to 1100 nm and there was a notch filter which blocked light around 390 nm making the resolvable cutoff around 390 nm. Some of the materials however, broadened past 390 nm. In Table 3.2 if a materials supercontinuum extended past the spectrometer cutoff it is labeled as, <390, meaning the supercontinuum extends lower than 390 nm.

**Table 3.2 – Spectral broadening in the bulk windows tested.**

<b>Material</b>	<b>Bandwidth [nm]</b>
SF5	490-1005
SF11	529-1005
B270	416-1019
BK7	412-1007
Fused Silica	<390-1016
SK11	400-1032
CaF <sub>2</sub>	<390-1002
KCL	406-1004
MgF <sub>2</sub>	<390-1007
Quartz	<390-1026
Laser	773-780

### 3.3 Conical Emission

Conical emission is the ring pattern that surrounds the central white-light continuum as depicted in Figure 3.2. Initial theories including self-phase modulation, four-wave mixing, and Raman were not enough to explain this phenomena [31]. The mechanism for this effect has been proposed to be a Cerenkov-like effect accompanying self-focusing [31]. Later studies from Reference 31, show a more qualitative explanation of the effect where the concentric ring pattern starting with the highest wavelength (red) in the innermost ring and going to lower wavelengths (blue) in each successive ring. If this was a result of four-wave mixing, the rings would appear in opposite order, blue to red. Another observation was wavelengths higher than the pump wavelength did not appear in the ring pattern. The conical emission was also found to be independent of focusing conditions, pulse length or intensity. Finally, experiments also showed that SCG was initiated by filamentation [31], but later studies have shown that this does not satisfy some experimental observations. Chin *et al.* propose that the conical rings present with SCG are another form of self-phase modulation (SPM) and explains how SPM can be described in a radial direction. This modified SPM also provides the proper shift of wavelength from the inner most rings being red to the outmost being blue [32].

In order to generate conical emission, 5  $\mu$ J pulses around 155 fs were focused into the samples using an  $f/35$  system and viewed by placing a screen 11.3 cm after the sample. Digital photos of the continua and rings were taken and can be seen in Figure 3.8.

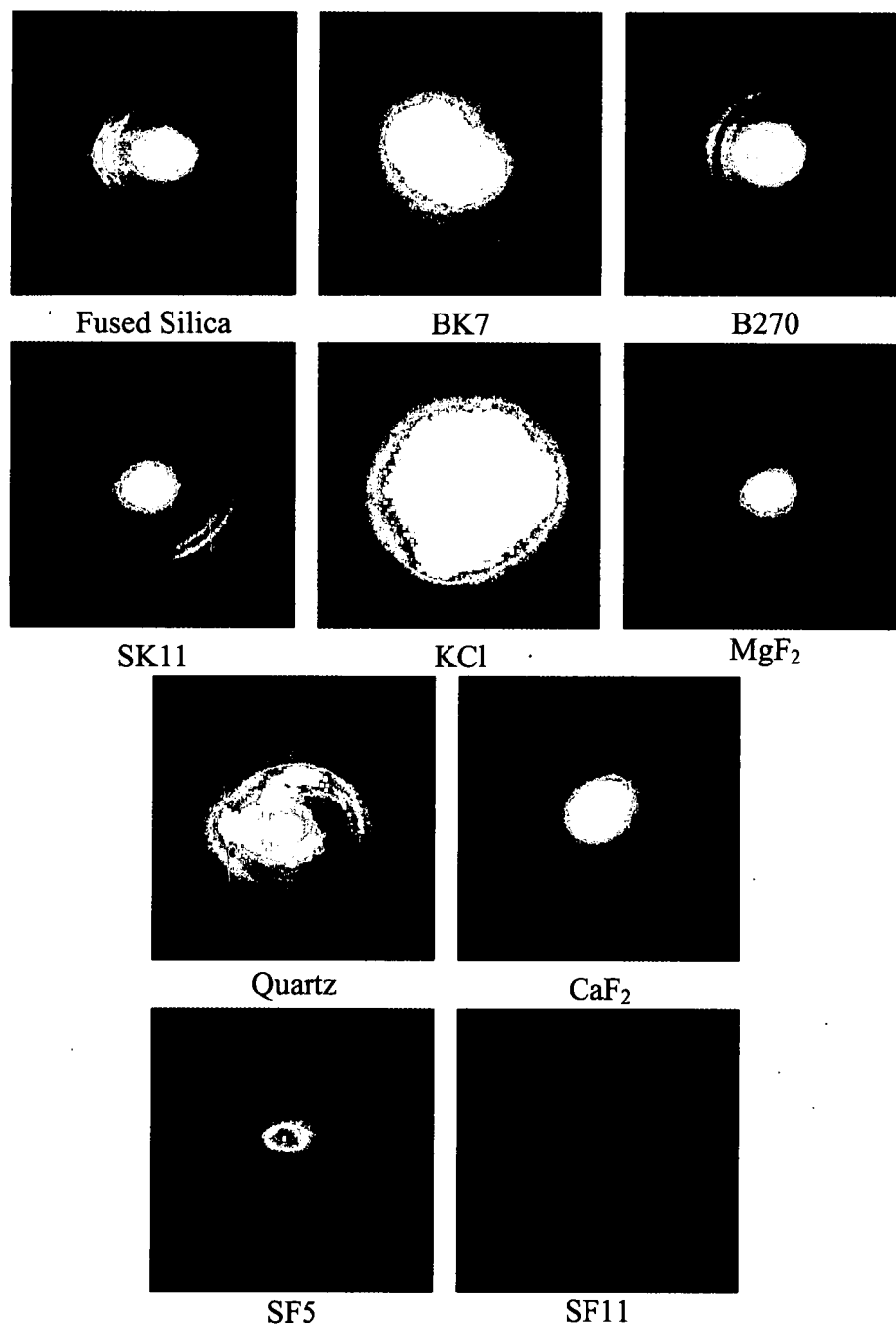


**Figure 3.8 – Supercontinuum generation along with conical emission in the crown, ionic, and flint samples after propagating 11.3 cm in air after the material.**

The angle at which the first concentric ring diverges was measured to be 4.0 degrees and found to be constant among the entire samples tested where effect was observed. Here the diffraction angle was measured by taking the center line profile of the red portion of

the .jpg image. The line profile for the conical emission in fused silica can be seen in Figure 3.9. This line profile was generated using the mathematics package Matlab®.

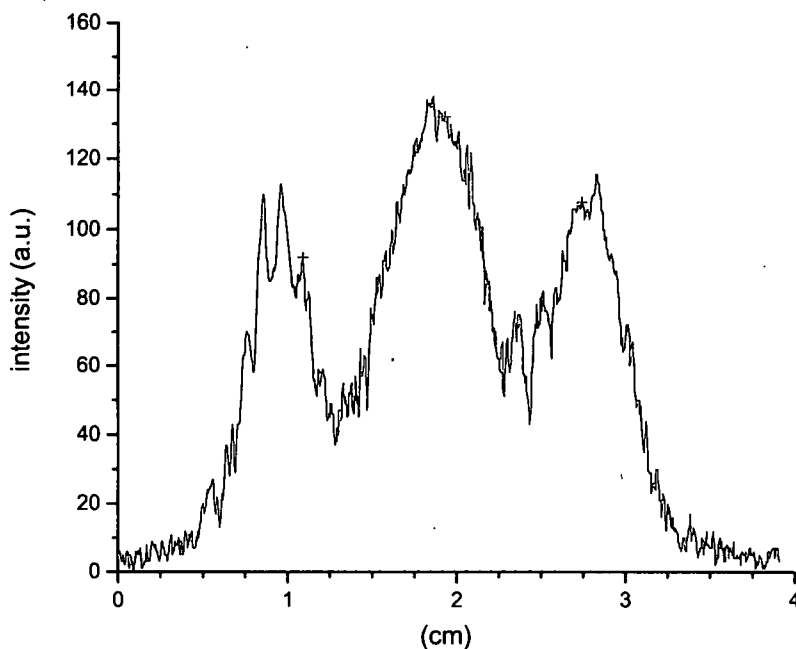


**Figure 3.9 – Center line profile of fused silica continuum seen in Figure 3.8.**

A summary table of the diffraction angle of the first conical ring can be seen in Table 3.3. The diffraction angles are quite constant which also verifies that the material type also plays a minimal roll in conical emission propagation. Also note that in the flint glasses where SCG is weak, conical emission was not present. Conical emission was only found in materials whose band gaps were above 3.9 eV.

**Table 3.3 – Summary table of the observed conical emission angle in the ten samples tested**

<b>Material</b>	<b>Conical Angle [Degrees]</b>
SF5	N/A
SF11	N/A
B270	4.0
BK7	4.1
Fused Silica	4.1
SK11	4.0
CaF <sub>2</sub>	4.8
KCL	4.9
MgF <sub>2</sub>	3.7
Quartz	4.0

### **3.4 Supercontinuum Threshold and $f/\#$ Dependence**

A property unique to materials is the supercontinuum turn-on threshold. It is generally accepted that SCG coincides with self focusing collapse (see Equation (3.1)) [19, 24], but in order to determine the critical power, the nonlinear index of refraction  $n_2$  must be known. Also it is now known that self-focusing is not the only mechanism which contributes to the onset of SCG others include: self-phase modulation, self-steepening, and multi-photon absorption. This section describes how the different materials supercontinuum was measured and what their threshold values were when exposed to three different focusing conditions.

Numerical aperture dependence of SCG has been documented and shown that as the numerical aperture (NA) increases the continuum threshold increases in fused silica [33]. Simply put, as the NA increases the interaction length within the sample decreases

and therefore less chance for SCG. The NA is inversely proportional to the  $f/\#$ , as seen below

$$NA = \sin(\tan^{-1}(f_{\#}^{-1})). \quad (3.2)$$

Therefore as the  $f/\#$  decreases the continuum threshold will increase, this trend will be shown.

The SCG threshold was measured by subjecting the materials to a fluence range from  $6 \text{ mJ/cm}^2$  to twenty-five percent above the continuum turn on, at  $\sim 7 \text{ mJ/cm}^2$  intervals for three different  $f/\#$ 's,  $f/9$ ,  $f/18$ , and  $f/35$  which correspond to NA's of 0.11, 0.055, and 0.029 respectively. Continua spectra were also taken as a function of increasing fluence to track any spectral broadening. Figure 3.10 shows an example of how until the supercontinuum turns on with increasing input fluence. A fused silica sample was used in this test.

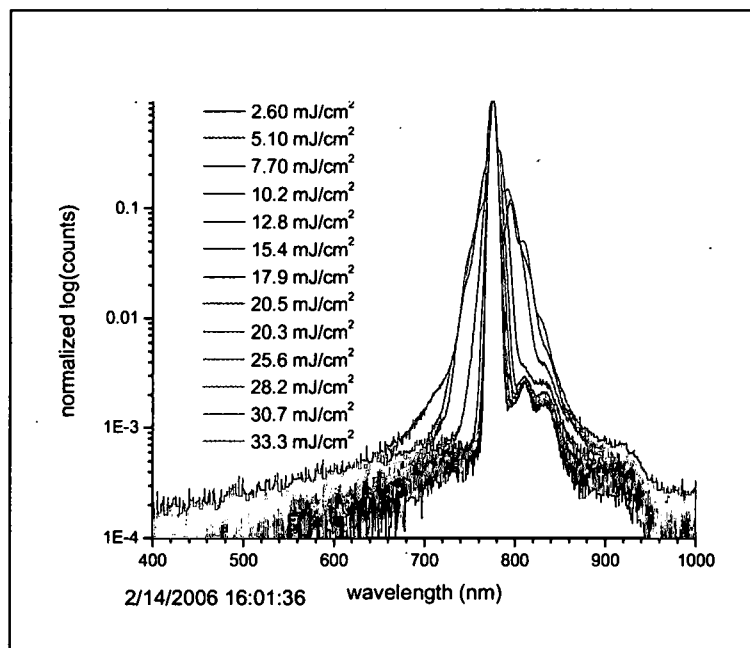


**Figure 3.10 – Spectra taken to determine the supercontinuum threshold in fused silica.**

As soon as the SC turns on it saturates the Raman effects seen in the fiber at lower peak energies. Once the spectra were collected for each sample, the standard deviation of the spectrum was determined, using the equation shown below to ensure all points are weighted evenly

$$\sigma = \sqrt{\frac{1}{n} \sum_i^n I_i (x_i - \bar{x})^2} . \quad (3.3)$$

A full width half maximum method or a similar method does not account for small fluctuations near the noise floor, evaluate an asymmetric spectrum evenly, and it only looks at the bandwidth at one part of the spectrum. Therefore, the standard deviation method is superior. The standard deviation, or rms bandwidth, is then plotted versus input fluence. The threshold is determined by linearly fitting the data before and after the white light turns on and examining where they intersect. A typical plot can be seen below in Figure 3.11. Although this technique works well, it should be noted that the broadening of the peak is weighted more heavily than in the wings. Hence it might make sense in future measurements to define thresholds specific to one's application. For example, when looking for the blue pedestal turn-on, it might be more sensible to measure the signal for frequencies on the blue-side of the input beam and exclude the initial spectral region around the pump wavelength. Other applications may be more interested in the red portion of the spectrum. In any case, the method shown here gave a good indication of where all of these processes turn on. A more specific threshold definition to a particular process will not have a significantly different threshold level than what was found using this technique.

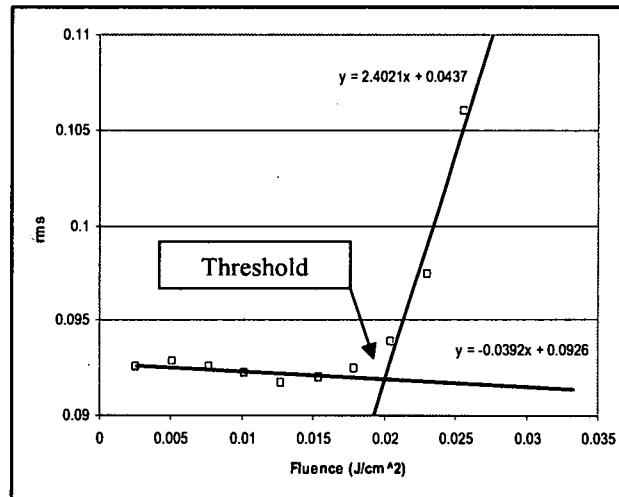


Figure 3.11 – SCG threshold data for fused silica using an f/35 lens.

Table 3.4 shows a summary of all the thresholds measured for each of the samples. As mentioned earlier, the continuum threshold increases as the  $f/\#$  decreases.

Table 3.4 – SCG threshold summary. For the flint glasses 6.52 and 10.4  $\text{mJ}/\text{cm}^2$  were the lowest detectable fluence levels for their respective focusing conditions.

	f/35	f/18	f/8.8
Material	Threshold [ $\text{mJ}/\text{cm}^2$ ]	Threshold [ $\text{mJ}/\text{cm}^2$ ]	Threshold [ $\text{mJ}/\text{cm}^2$ ]
SF5	< 6.52	< 10.4	30.4
SF11	< 6.52	< 10.4	30.4
B270	32.9		
BK7	45.3	59.3	104
Fused Silica	50.9	81.1	117
SK11	31.1	50.0	
CaF <sub>2</sub>	69.6	89.5	205
KCl	23.7		
Quartz	38.2		
MgF <sub>2</sub>	118		

The above summary leads to some interesting materials properties. The flint glasses, while they had the shortest spectral broadening, they exhibit turn-on thresholds at fluence



levels that were below our detection capabilities of our joulemeter for  $f/35$  and  $f/18$  systems. One of the ionic glasses,  $\text{MgF}_2$ , has twice the continuum threshold of any other material tested. This would be a good glass to use in an optical system that which would be subject to high fluence levels where SCG is not desired.

### 3.5 $f/\#$ Spectral Dependence (with Photos)

The previous section showed how SCG thresholds depend on the  $f/\#$  of the system. In this section, it will be shown that the spectra and observable continua pattern also are affected by changes in  $f/\#$ . One window from each category was selected, fused silica,  $\text{CaF}_2$ , and SF11. The continua were measured at a constant fluence level of  $326 \text{ mJ/cm}^2$ , well above their respective thresholds. The effects seen in the following figures can be attributed to similar effects described above. As the  $f/\#$  decreases the depth of focus inside the material the interaction length within the sample decreases making the spectral broadening smaller [33]. The following Figures 3.12 through 3.14 show this  $f/\#$  dependence. Not only does the broadening decrease, but the conical emission is not present in the ionic crystals and crown glasses as the  $f/\#$  decreases. This effect can be seen in the photos adjacent to the spectra.

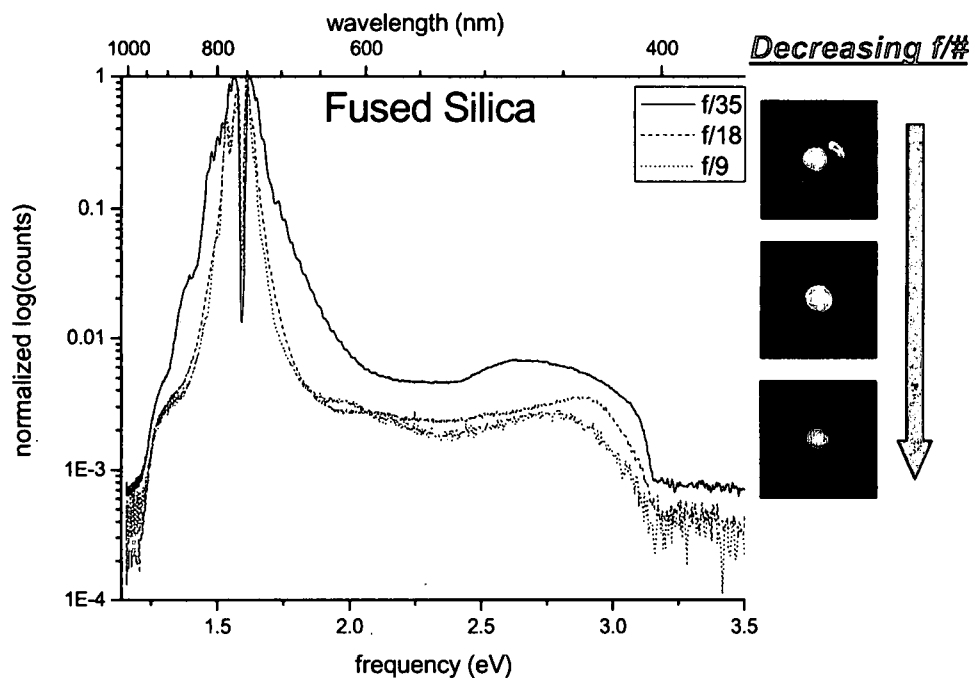


Figure 3.12 – SCG in fused silica at 326 mJ/cm<sup>2</sup> at three different f/#'s plus digital photos of the continua after propagating 11.3 cm past the sample.

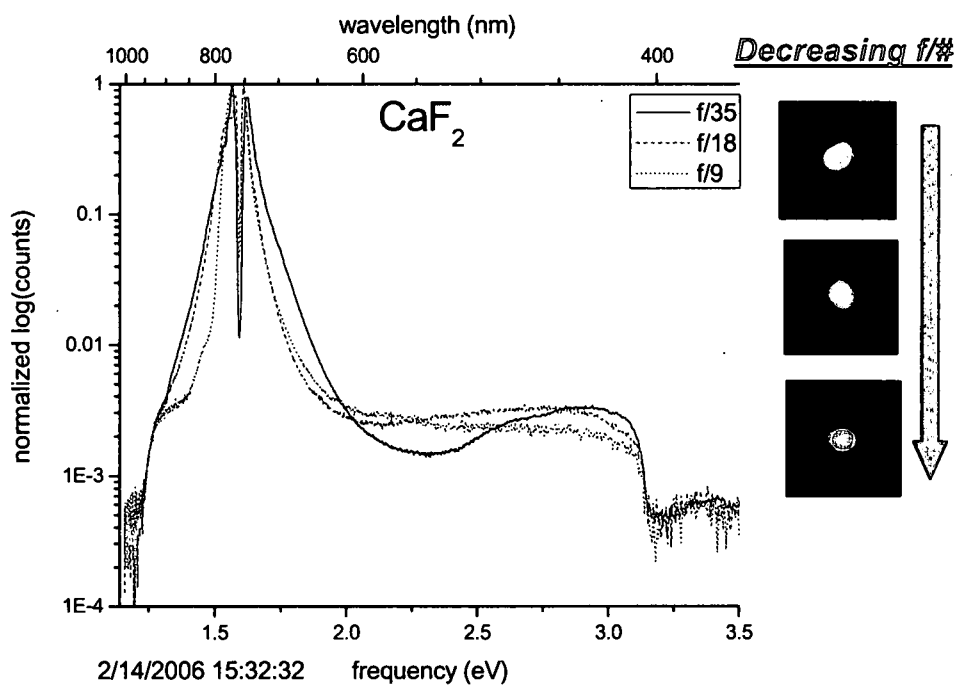


Figure 3.13 – SCG in CaF<sub>2</sub> same focusing conditions as above.

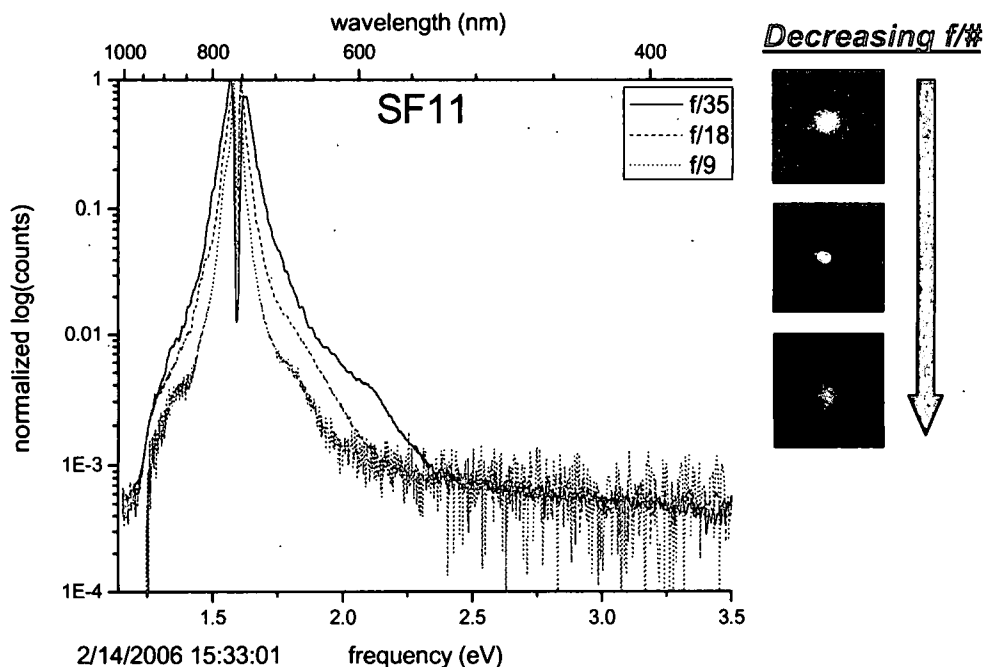


Figure 3.14 – SCG in SF11 same focusing conditions as above.

### 3.6 Sample Thickness Dependence

In this section, three samples of different thickness of B270 were tested to find the sample thickness dependence. Up until this point all the samples tested were 3 mm thick. Samples of the crown glass, B270, of thicknesses of 1, 2 and 3 millimeters were used. As before, when the interaction length was changed due to  $f/\#$ , the spectra were altered. This time the interaction length was changed due to sample thickness. Figure 3.15 shows the change in the spectra from the 3 millimeter sample to the 1 millimeter sample. The spectrum of the 2 millimeter sample is not very different from the 3 millimeter, but when the overall path length is 1 millimeter the SCG is drastically affected. In the 1 millimeter sample, the interaction length is much smaller causing a lot less SCG within the material. A model for the dependence on interaction length has yet to be determined, but for this

focusing condition there seems to be a drastic change in the spectral broadening from the 1 to 2 mm sample.

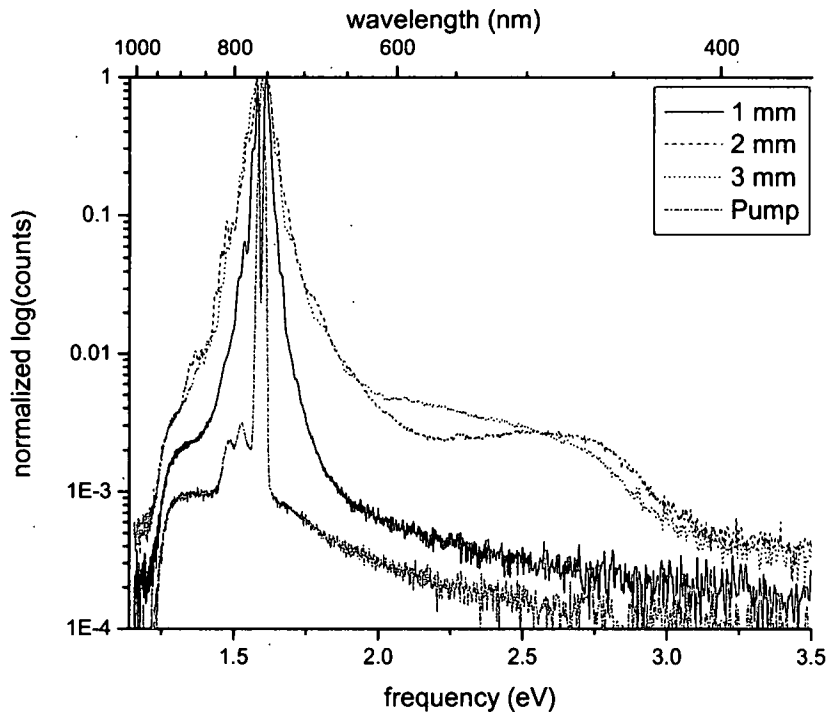


Figure 3.15 – SCG in three different thicknesses of B270 at  $326 \text{ mJ/cm}^2$  using an f/35 system.

### 3.7 Backward Emission

Until now, all of the supercontinuum effects have been measured and observed in the forward direction, but supercontinuum is not limited to only forward propagation – it also travels backwards. The backward emission is due to the nonlinear mechanisms at work. If four-wave mixing is one of the mechanisms for continuum generation, then in the presence of phase matching k-vectors could point in the direction opposite of propagation. Another possibility is a significant increase in the index, similar to that found in air, causing a sharp increase in Fresnel reflections [34]. This effect is not well

understood in solids and is a topic open for research. Extensive research on this effect has not been performed making backwards continuum generation far from being completely understood.

The backwards propagation is hard to see without blocking the pump beam. In order to view it, an iris was placed before the sample and stopped down such that it allowed enough laser light to pass through and still generate continua. Two photos of the backward emission were taken and can be seen in Figure 3.16. Since the continuum is traveling backwards and collinear to the incoming pump beam only the outermost edges of the backward SC are seen. The backward continuum is only seen on one edge of the iris due to slight mis-alignment of iris. If the backward continuum could be viewed it would diffract similar to normal, forward SCG.



**Figure 3.16 – Backwards SCG emission in fused silica (left) and quartz (right). The images have been brightened so the effect can be seen easier.**

## CHAPTER 4

### Supercontinuum Simulations

Supercontinuum is still not a completely understood nonlinear process, but many of the mechanisms that contribute to white-light generation are known. One of the main reasons SCG is not understood is because there are several competing nonlinear processes at work, and knowing how these effects interact together is difficult to manage. Also, for femtosecond pulses purely linear effects like group velocity dispersion is important since there is so much bandwidth. The time and space dependence femtosecond pulse propagation do not tend to stay independent of each other, they get coupled together making it more complicated than a continuous wave or long pulse problem. A model was generated to simulate pulse propagation through a nonlinear medium. This model uses a modified nonlinear Schrödinger equation (NLSE). The NLSE uses the following terms to simulate the effects of SCG: diffraction, space-time focusing, dispersion, Kerr effect, self-steepening, and multi-photon absorption. Each one of these terms contributes differently to the final continuum spectrum. The goal of this model is to successfully predict the shape and dependence of the different terms used in the NLSE for SCG by simulating the output spectrum in a nonlinear medium.

#### 4.1 Mechanisms for SCG

Nonlinear optical effects stem from the fact that all materials do not respond purely linearly to applied light. At appreciable intensities (i.e. focused laser beams), a higher order term in the index of refraction begins to turn on. This nonlinear index of refraction is intensity dependent and its behavior is given by:

$$n = n_0 + n_2 I, \quad (4.1)$$

where  $n_0$  is the linear index of refraction,  $n_2$  is the nonlinear index of refraction and  $I$  is the intensity. This is a nonlinear optical effect driven by third order susceptibility,  $\chi^{(3)}$ . The nonlinear index,  $n_2$ , can be defined in SI units as [23]

$$n_2 = \frac{3\chi^{(3)}}{4n_0}. \quad (4.2)$$

This small change in the index of refraction causes propagation effects like self-focusing and self-phase modulation, which are main mechanisms for SCG.

Self-focusing results directly from the intensity dependent nonlinear index of refraction defined in Equation 4.1. In most materials,  $n_2$  is positive resulting in a higher index of refraction at the center of the beam compared to the edges. This results in the refractive index acting like a positive lens and focusing the beam as it propagates through the medium. At high enough intensities the beam becomes very unstable and breaks down due to small variations across the beam's spatial profile and leads to filamentation in the medium. The critical power can be defined as the point where self-focusing exceeds diffraction and for a continuous wave beam the collapse is given by Equation 3.1 [35]. Self-focusing can also act as a negative lens in a material which has a negative nonlinear index of refraction and the beam will diverge instead of collapse.

A laser beam will not self-focus in a material indefinitely. Once the self-focused beam reaches a certain size and intensity other processes such as ionization becomes important and introduce a negative nonlinear refractive index that cancels out the lensing behavior. This leads to plasma formation inside the medium which defocuses the beam and essentially stops self-focusing. Another effect that slows self-focusing is diffraction. Once the beam gets too small it wants to diffract which ends up offsetting self-focusing in the medium. Coupled together, these competing processes contribute to SCG.

Another effect that has been characterized as the dominant mechanism to trigger SCG is self-phase modulation (SPM). SPM is a temporal analog to self-focusing. When dealing with short pulses, intensity is also time dependent. Thus the nonlinear refractive index is also time dependent, creating a nonlinear phase of the pulse. If a pulse propagates through medium of length,  $L$ , it accumulates a phase,  $\phi$ , defined by,

$$\phi(z, t) = (kL - \omega t), \quad (4.4)$$

where  $k$  is the wave number,  $\omega$  is the frequency and  $t$  is the time. Expanding Equation 4.4, the nonlinear phase can be written to include the nonlinear index of refraction as follows

$$\phi_{NL} = \frac{\omega L}{c} (n_0 + n_2 I(t)) - \omega t, \quad (4.5)$$

where  $c$  is the speed of light equal to  $3.0 \times 10^8$  m/s. The instantaneous frequency term will show the effect of SPM due to dispersion across the temporal profile of the pulse. The instantaneous frequency term is defined by the negative time derivative of Equation 4.5, so it can be written as

$$\omega(t) = \omega - \frac{n_2 \omega L}{c} \frac{\partial}{\partial t} I(t). \quad (4.6)$$



The negative time derivative creates a red shift on the leading edge and a blue shift on the trailing edge in the instantaneous frequency. Figure 4.1 shows SPM's ability to broaden a pulse in a material which has an appreciable nonlinear index of refraction.

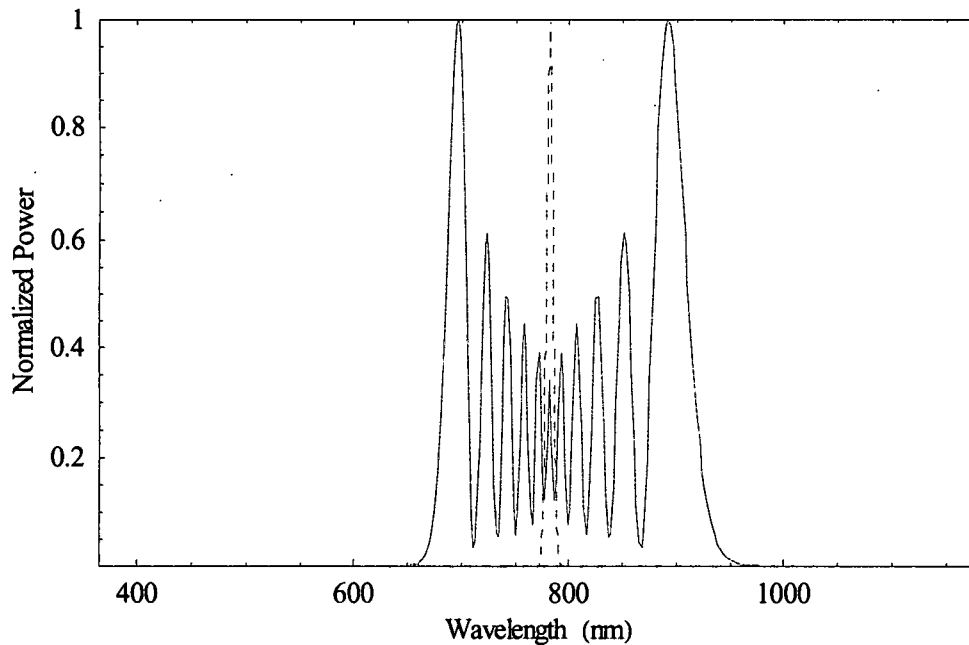


**Figure 4.1 – Plot showing the effects of SPM (red, solid) on an incident 100 femtosecond laser pulse (blue, dashed) propagating through fused silica [23].**

As the phase velocity was influenced by the nonlinear refractive index, the group velocity is also affected. Group velocity exhibits the same intensity dependence as the phase velocity. As the pulse propagates through the medium, the peak of the pulse experiences the highest index of refraction, thus slowing down relative to the wings of the pulse. Since the top of the pulse slowed down this leads to an increased slope of the trailing edge of the pulse. The change to the pulse envelope is known as self-steepening. This dramatic shift is often called an “optical shock” which through its influence on SPM has been said to be the cause of the blue pedestal seen in typical super-continuum spectra [36].

Another mechanism which plays a role in continuum generation is space-time focusing. This is a linear propagation term which determines that the front and back of the pulse diffract in different ways. Without space-time focusing, it was shown that a femtosecond pulse will break up into two pulses before the onset of self-focusing [37]. Including the space-time focusing term causes the pulse to develop a trailing optical shock before a pulse splitting effect occurs [38]. It is important to include this linear term since it is a more adequate explanation of what is really happening in the medium where self-focusing is present. Moreover, pure self-focusing is never present in propagation alone, it is always accompanied by other competing effects.

Multi-photon absorption is another mechanism which limits the effect of self-focusing. Multi-photon absorption produces carrier band electrons (i.e. free carriers) that cause a net decrease in the index of refraction and creates a negative lensing effect which controls the self-focusing. This effect also modulates the phase and enhances SPM which has shown to generate the blue pedestal seen in SCG [18]. An interested reader can review the work of Keldysh to understand the complete theory [39]. Avalanche ionization is another nonlinear effect which contributes to SCG. It is a lot like multi-photon absorption. Band to band transitions cause a negative lensing effect counteracting self-focusing which prevents the pulse from completely collapsing.

#### **4.2 Modified Nonlinear Schrödinger Equation**

The model includes all of the terms described in the previous section. A modified nonlinear Schrödinger equation (NLSE) is used to model the beam propagation through a

nonlinear medium. A one dimensional space and time model was developed to simulate SCG. An input Gaussian pulse is used of the form

$$A(z, t) = A_0 e^{-\frac{z^2}{2w_0^2} - \frac{t^2}{2\tau_p^2}}, \quad (4.7)$$

where  $A_0$ , is the amplitude,  $w_0$  is the transverse spot size, and  $\tau_p$ , is the pulse width. This equation for propagation along the z-direction can be expressed as [36],

$$\begin{aligned} \frac{\partial A}{\partial \zeta} = \frac{i}{4} & \left( \overbrace{\hat{1}}^{\text{Diffraction}} + \overbrace{\frac{i}{\omega\tau_p} \frac{\partial}{\partial t}}^{\text{Space-time focusing}} \right)^{-1} \nabla_{\perp}^2 A - i \overbrace{\frac{L_{df}}{L_{ds}} \frac{\partial^2 A}{\partial \tau^2}}^{\text{Dispersion}} + i \left( 1 + \overbrace{\frac{i}{\omega\tau_p} \frac{\partial}{\partial \tau}}^{\text{Self-steepening}} \right) \\ & \left( \overbrace{\frac{L_{df}}{L_{nl}} |A|^2 A}^{\text{Kerr effect}} - \overbrace{\frac{L_{df}}{L_{pl}} \left( 1 - \frac{i}{\omega\tau_c} \right) \rho A}^{\text{Plasma effects}} + i \overbrace{\frac{L_{df}}{L_{mp}} |A|^{2(m-1)}}^{\text{Multi-photon absorption}} \right) \end{aligned} \quad (4.8)$$

where  $L_{df} = k w_0^2 / 2$  is the diffraction length,  $L_{ds} = \tau_p^2 / \beta_2$  is the dispersion length,  $L_{nl} = c / \omega n_2 I_0$  is the nonlinear length,  $L_{pl} = 2 \rho_0 / \sigma \omega \tau_c$  is the plasma length, and  $\rho_0$  is an electron density. Furthermore,  $\sigma$  is an inverse Bremsstrahlung cross section constant,  $L_{mp} = 1 / \beta^{(m)} I_0^{(m-1)}$  is the multi-photon absorption length, and  $\beta^{(m)}$  is the multi-photon absorption length. The normalized distance is  $\zeta = z / L_{df}$ , the normalized retarded time is  $\tau = (t - z / v_g) / \tau_p$ , and the intensity is defined as  $I_0 = n_0 c |A_0|^2$ . In the plasma length term,  $\rho$  can be defined as the following [36],

$$\frac{\partial \rho}{\partial \tau} = \overbrace{\alpha \rho |A|^2}^{\text{Avalanche ionization}} + \overbrace{|A|^{2m}}^{\text{Multi-photon absorption}}, \quad (4.9)$$

where  $\alpha = \sigma I_0 \tau_p / n_0^2 E_g$  is the avalanche ionization coefficient,  $E_g$  is the band-gap of the material. The previous rate equation includes the effects of avalanche ionization and multi-photon absorption [36]. The terms have been label in Equations 4.9 and 4.10 so that each term can be clearly identified. This model was originally devised by Gaeta [36], but it has been modified slightly to include the beam parameters used in this research. The only effect not included in the model is the effect of self-steepening on the plasma effects in Equation 4.9. This effect was omitted because it could not be solved for due to the nature of the algorithm. This model was used to propagate an input pulse in sapphire using a split-step method written in MatLab®. The code can be seen in Appendix A.

### 4.3 Supercontinuum Simulations

This is a preliminary model which has proven to be a good start to reproduce essential qualitative features of SCG and allow specific mechanisms to be isolated and examined. The model is (1+1) dimensional model, one transverse dimension in time, and with one dimension Cartesian symmetry in space. This model can be used to simulate a femtosecond laser pulse propagating through a medium under certain focusing conditions. The focal length of the lens used in the simulation is the same as that used in the experiment above to generate white-light continua in the transparent samples. Since this is a (1+1) dimensional model the self-focusing collapse behaves slightly different than it would in a model with radial symmetry, but this model exhibits the essential effects.

The results from this model include the on-axis peak power through the sample, the (1+1) dimensional final intensity spectrum, and the final spectrum. The sample modeled was sapphire. This sample was modeled because of the complete list of nonlinear material properties [36]. The coefficients used in Equations 4.8 and 4.9 can be seen in Table 4.1

**Table 4.1 – Coefficients used in nonlinear SC model.**

$\lambda$ [ $\mu\text{m}$ ]	$\tau_p$ [fs]	$L_{ds}$ [cm]	$L_{df}$ [cm]	$L_{nl}$ [cm]	$L_{pl}$ [cm]	$L_{pm}$ [cm]	$\alpha_k$	$\alpha$	m
0.8	150	18	80	3.3	8000	8000	5	0.1	5

The on-axis peak power shows how pulse is focusing in the medium. An example of this can be seen in Figure 4.2.

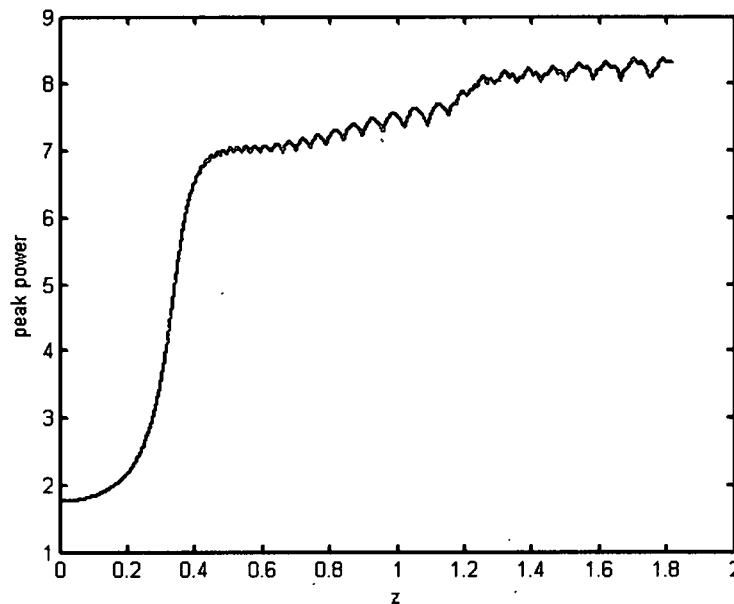


**Figure 4.2 On-axis peak power as the pulse propagates through sapphire. The z-distance is scaled to the diffraction length so it does not have physical units.**

Here the peak power increases rapidly as predicted due to the Kerr nonlinearity and self-focusing. In (2+1) dimensional models, the on-axis peak power increases significantly more due to the dimensionality of the transverse effects in this model. The final intensity spectrum shown in Figure 4.3 shows the off-axis conical emission seen in the experimental results. Wavelengths in the blue pedestal are present can also be seen on axis from this graph, but since they are so much weaker they are hard to see in Figure 4.3. The final spectrum will show these higher frequency terms better. Figure 4.3 has been scaled to physical units of wavelength and angle so the plot is more intuitive. The off-axis red peaks occur around 2.5 degrees which is similar to conical emission angle observed in the experiment. There are other red peaks that occur further off-axis which are additional conical rings. You can also see that conical emission does exist at other wavelengths but compared to the red emission it is comparably weaker. Of course this is just a (1+1) dimensional model so the off-axis diffraction could be slightly different in a three dimensional model where the pulse collapse is more consistent with actual experimental results.

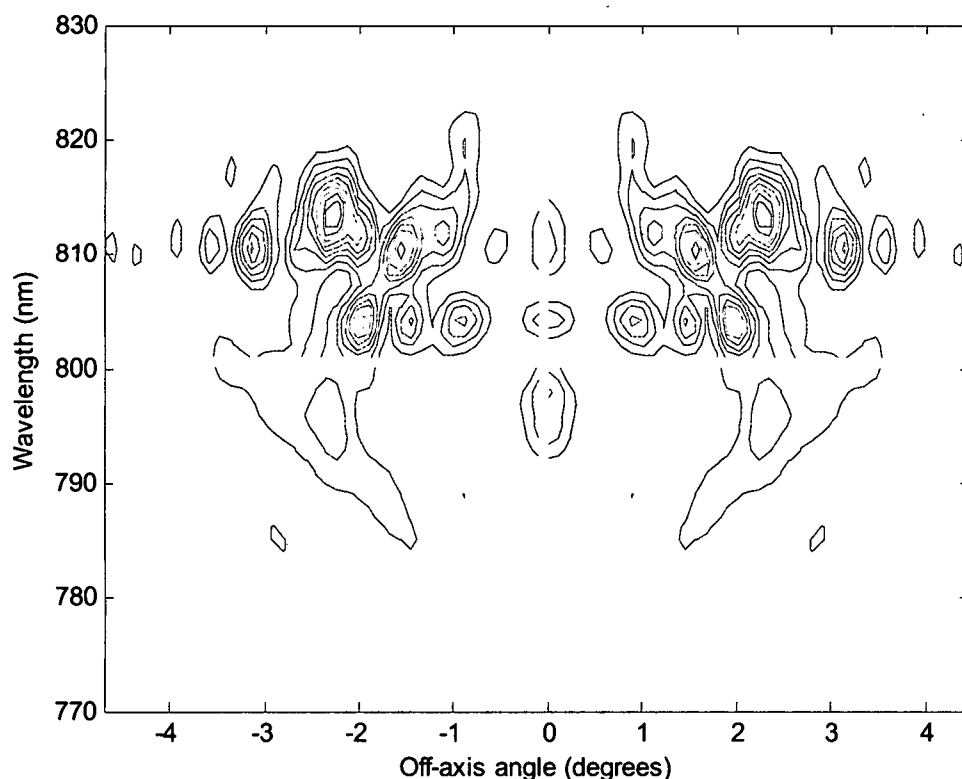


**Figure 4.3 – Final intensity spectrum of the pulse propagated through sapphire.**

The final spectrum plotted in Figure 4.4, this plot shows the extended blue pedestal and the spectral broadening about the center wavelength. Since wavelength does not scale linearly with frequencies the wavelength scale in Figure 4.4 can only extend down to 600 nm. Adding frequency points to the FFT would extend this range further but would lengthen the run time of this (1+1) dimensional model. The blue pedestal is only down one order of magnitude compared to the peak of the spectrum whereas in the experimental data it was shown that it was typically down at least two. This preliminary model does show the dramatic effect of these nonlinear terms used in Equation 4.8. The Kerr effect was strong enough to cause the self-focusing the trigger nonlinear propagation effects, such effects as enhanced SPM due to self-steepening and space-time focusing.

These mechanisms led to the extended blue pedestal seen in Figure 4.4. This is an example of what can happen to the spectrum as a pulse is propagated through a nonlinear medium with high intensities involved.

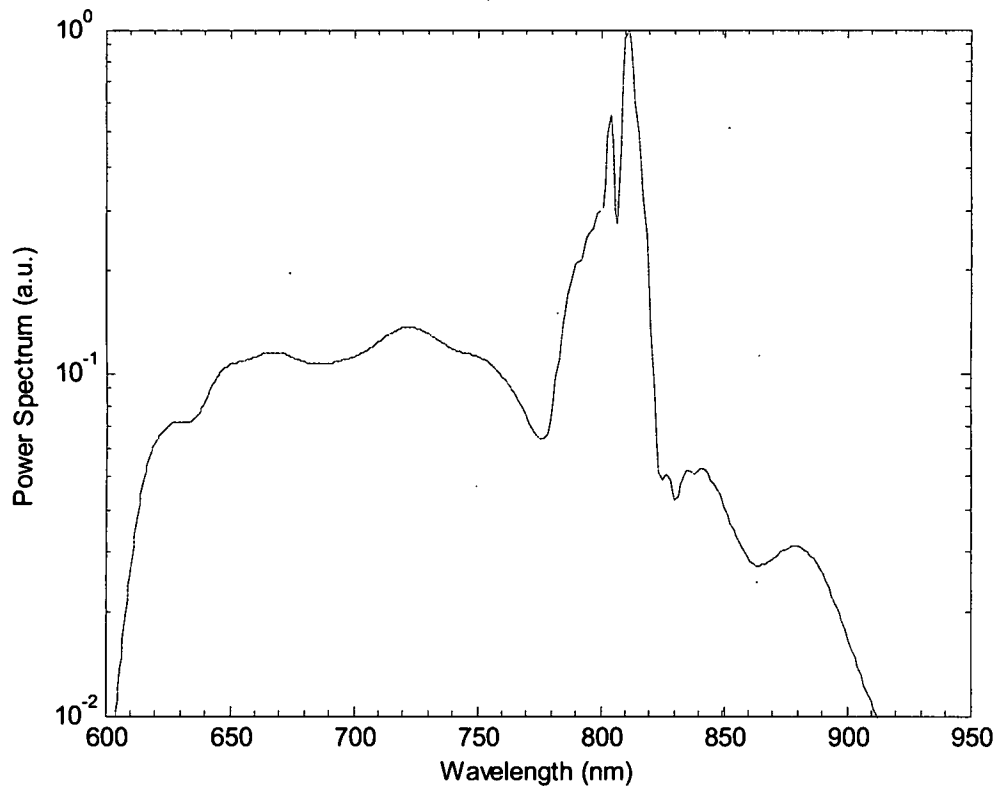


**Figure 4.4 – Simulated SC spectrum with a 800 nm pump and at 150 fs.**

The previous simulations the nonlinear terms including the Kerr effect, plasma effects, and multi-photon absorption all were included. Additional simulations were run in which the only nonlinear effect was due the Kerr index and one simulation with Kerr and plasma terms present. None of the other input parameters were changed in these additional simulations. The other nonlinear terms not included were set to zero. The simulation with the Kerr term being the only nonlinear present failed to yield a solution. The pulse envelope simply became unstable due to the algorithm and yielded no



mathematical solution. Physically this makes sense in that we expect self-focusing in the absence of competing effects it will go to an extreme limit. In real systems this is where a filament forms. Since there were no compensating effects of plasma formation and multi-photon absorption self-focusing dominated the solution to the NLSE. Another simulation was run with the nonlinear effects due to Kerr and plasma effects. This simulation had a solution but it led to excessive diffraction such that the output overfilled the spatial grid set up in the simulation. Hence we can conclude that the plasma formation does indeed cause the beam to diffract. In order to isolate the various nonlinear effects contributed by each term in the NLSE the input parameters and the grid size would need to be changed and perhaps a smaller sample thickness used such that the solutions would show a qualitative picture without extraneous artifacts.

## CHAPTER 5

### Infrared Material Study at 1550 nm

The materials studied in this chapter are bulk semiconductor materials. When exposed to large enough intensities these materials exhibit third order,  $\chi^{(3)}$ , nonlinear effects. Semiconductors have become a valuable tool in the optical community being used in lasers, switches, and many other optical devices. Many of these nonlinear material properties were previously measured using cw, nano, or pico-second laser pulses. The measurements made with these longer pulses can introduce other effects in the materials such as thermo-optic or electrostriction absorption or refraction due to nonlinearly excited free-carriers [40]. Using femtosecond pulses can eliminate some of the ambiguities that are present using longer pulses because the turn on time for the effects is greater than 100 femtoseconds. In this experiment femtosecond laser pulses at 1550 nm were used to measure the nonlinear absorption coefficients in three bulk semiconductor materials Si, CdTe, and InP. The source for this experiment will be the idler beam of the OPA.

#### 5.1 Nonlinear Absorption

All semiconductor materials usually exhibit some linear absorption ( $\alpha$ ) in the infrared range. Linear absorption can be described as a material not being completely

transparent over an optical path length at a given wavelength of light, and is due to material transitions caused by absorption of single photons whose energy ( $\hbar\omega$ ) exceeds the semiconductors band-gap energy ( $E_g$ ). The rate of transitions is  $\alpha I$  and only non zero when the frequency obeys  $\hbar\omega > E_g$ . When the intensity of light is strong enough, the linear approximation for the absorption is no longer adequate the transition rate acquires a term that is  $\alpha^2$  and non zero for frequencies  $\omega$  such that  $\hbar\omega \geq \frac{1}{2}E_g$  and the following expression must be used [40]

$$\alpha(I) = \alpha + \beta_2 I, \quad (5.1)$$

where  $\beta_2$  is the nonlinear absorption or two-photon absorption (TPA) coefficient. Figure 5.1 compares linear absorption versus TPA.

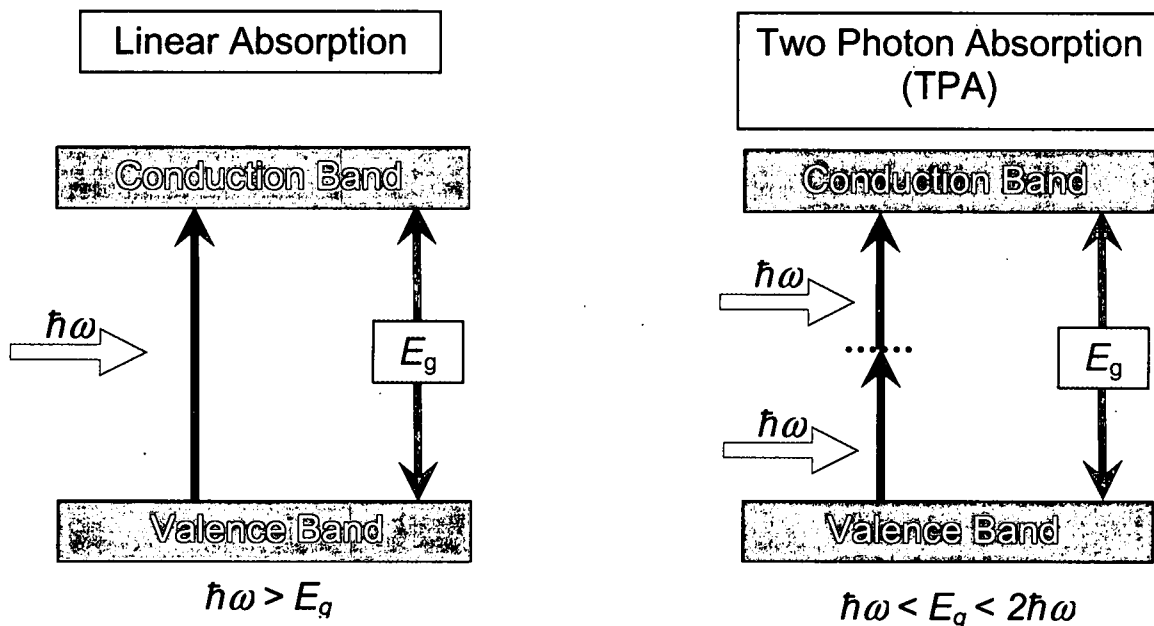


Figure 5.1 – Diagram illustrating the differences between linear and nonlinear absorption.

The nonlinear TPA coefficient is a cubic nonlinear effect mediated by the imaginary part of the third order susceptibility  $\chi^{(3)}$

$$\chi^{(3)} = \chi_R^{(3)} + i\chi_I^{(3)}. \quad (5.2)$$

The real part of  $\chi^{(3)}$  is related to the nonlinear index of refraction by,

$$\chi_R^{(3)} = 2n_0^2\epsilon_0cn_2, \quad (5.3)$$

and the imaginary part related to the two-photon absorption coefficient  $\beta_2$  by [40],

$$\chi_I^{(3)} = \frac{n_0^2\epsilon_0c^2}{\omega}\beta_2, \quad (5.4)$$

where  $\epsilon_0$  is the permittivity of free space  $\epsilon_0 = 8.85 \times 10^{-12}$  F/m,  $c$  is the speed of light  $c = 3.00 \times 10^8$  m/s, and  $\omega$  is the frequency of light.

In order to predict  $\beta_2$  using fundamental material properties, a simple quantum two-band model based on the Stark effect and bound-electronic response has been solved by Van Stryland *et al.* which predicts  $\beta_2$  [41]. This model can be used to predict  $\beta_2$  in direct-band gap materials based on parabolic band structure approximations and has been shown to predict values to within approximately 30 percent [41, 42]. The equation used to calculate  $\beta_2$  is shown below

$$\beta_2 = \frac{K\sqrt{E_p}}{n_0^2E_g^3} \left( \frac{2\hbar\omega}{E_g} - 1 \right)^{\frac{3}{2}} \left( \frac{2\hbar\omega}{E_g} \right)^{-5} \quad (5.5)$$

In this equation  $\hbar$  is Planck's constant divided by  $2\pi$ ,  $\hbar = 1.05 \times 10^{-34}$  m<sup>2</sup>kg/s,  $E_g$  is the band gap of the semiconductor, and  $K$  is a dimensionless fitting parameter. Furthermore,  $E_p$  is related to the Kane momentum parameter [42] and is approximately 21 eV for most

direct band-gap semiconductor materials. The constant  $K$  is equal to 1940 when  $E_g$  has units of eV and  $\beta_2$  has units of cm/GW [41]. This independent material constant,  $K$ , was used by Krauss and Wise when they studied semiconductor materials using femtosecond laser pulses [42]. Van Stryland *et al.* used picosecond pulses and used a value of 3100 for  $K$  [42]. Thus, the different values of  $K$  are based on the different pulse widths used.

The parabolic model also has additional restrictions on the incident photon energy, which must either be less than the band-gap energy but greater than half the band-gap energy, in other words must satisfy the following expression  $\frac{1}{2}E_g < \hbar\omega < E_g$ . If the incident energy does not satisfy this inequality, TPA will not be allowed [43]. This can be seen in terms of energy conservation by referring to Figure 5.1. This is a quick check to determine whether a material will exhibit significant TPA at the desired wavelength.

## 5.2 Experimental Setup and Results

A standard way to measure  $\beta_2$  uses the z-scan technique [40]. This technique is used by many to determine the TPA coefficients as well as the nonlinear index of refraction. The z-scan technique involves translating a sample (in the z-direction) along the axis of a loosely focused Gaussian beam so the sample sees a different intensity, spot size, and phase front at each z-position. This works well when the source is stable and easily characterized at every z-position. Unfortunately, when trying to implement this experiment using the OPA to measure the TPA coefficients in the semiconductor samples, many problems were encountered.

Instead of using the z-scan technique to measure  $\beta_2$ , a standard nonlinear transmission method was used. In this setup, the sample is placed at focus and then the incident energy is varied. This method reduces some of the uncertainty in the experiment since only one z-position has to be carefully profiled although it requires high dynamic range detection. The transmission through the sample at each incident energy is then recorded.

The laser source used for this experiment was the idler beam from the OPA which was tuned to 1550 nm. The OPA was only capable of producing 3  $\mu\text{J}$  of energy per pulse at this wavelength, therefore the range of intensities was fairly small. Since the energy range was so small by using three different lenses to focus the beam into the sample to generate a fairly large range of intensities were created. A 400 mm lens was used to generate a focused ( $1/e^2$  diameter) spot size of  $\sim 0.7$  mm, a 500 mm lens made a 2 mm focused spot, and a 750 mm lens generated a 3.5 mm spot size. A Spiricon 1550-M phosphorus coated CCD camera was used to profile the beam at focus, and the laser energy was attenuated using a half waveplate/polarizer combination. The wave-plate was rotated every two degrees from the maximum energy through the minimum. At each wave-plate angle the incident energy was measured without the sample, and then the sample was replaced and the transmitted energy was measured. The attenuator was able to give extinction of the laser down to the noise floor of the detector. The detector used was a pyroelectric joulemeter (Molelectron J3-09) with a 9 mm diameter active area and flat response in the near infrared. The joulemeter was placed 3 cm behind the sample to collect all the transmitted light. The overall experimental setup can be seen in Figure 5.2.

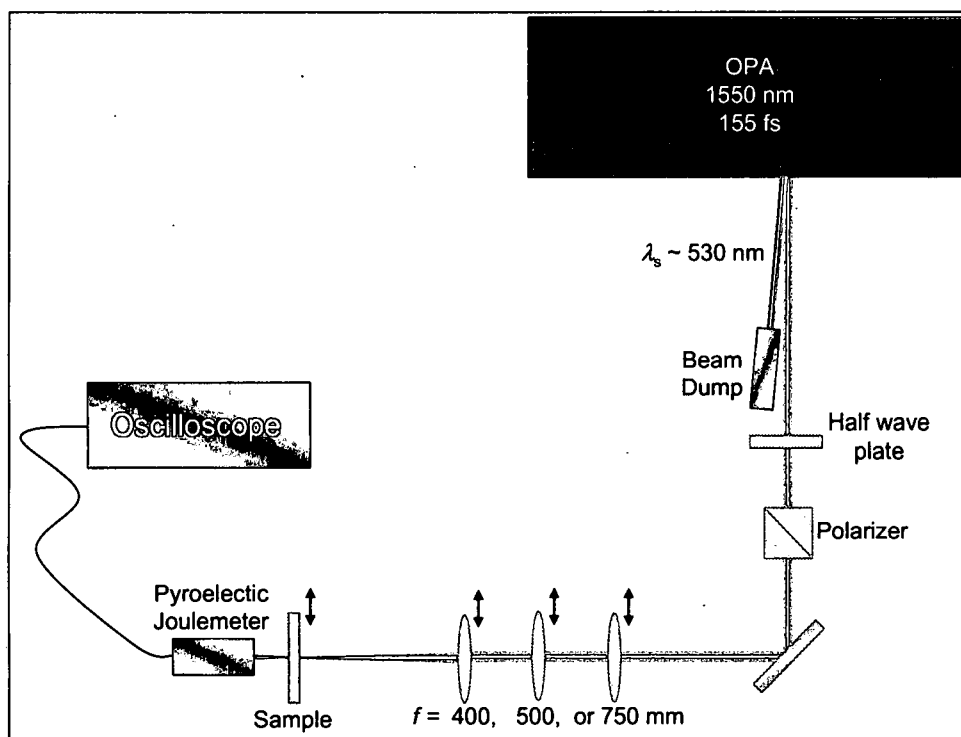


**Figure 5.2 – Nonlinear absorption experiment using the idler output of the OPA.**

An oscilloscope was used to measure the joulemeter output voltage, and at each wave-plate angle and 500 waveforms were averaged.

The nonlinear absorption,  $\beta_2$ , was measured for three semiconductor samples: bulk Si, CdTe, and InP. CdTe and InP are direct band gap materials where the two-band model will apply and the Si sample is indirect in nature and the model will not apply. In a direct band-gap material the valence and the conduction band correspond to the same momentum ( $k$ ). Meaning electrons can combine directly from the valence band to the conduction band while conserving momentum. In an indirect band-gap material the valence and conduction band require different momentums. This means, in an indirect band-gap material a phonon is also required to stimulate the transition from the valence band to the conduction band. Figure 5.3 illustrates the difference between the two band-gap states. [44]

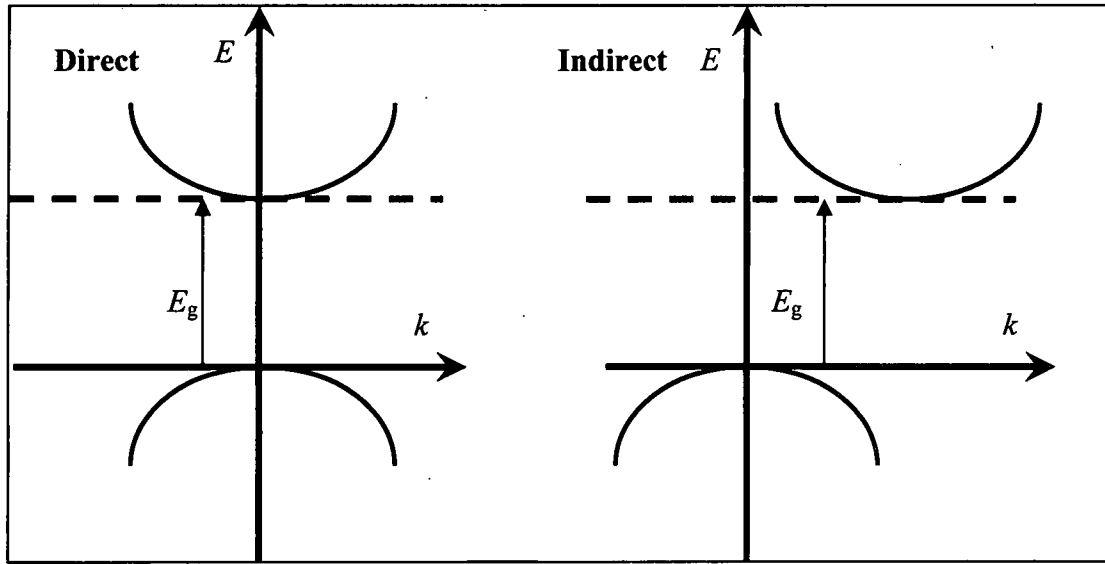


**Figure 5.3 – Diagram illustrating the difference between direct and indirect band-gap semiconductors.**

The transmission was determined over a range of intensities for these samples and normalized by dividing out the linear absorption which included losses from Fresnel reflections. The different lenses were used to cover enough intensities to generate a change in transmission of more than 20 percent. To determine the value for  $\beta_2$ , the fit used was that for a Gaussian pulse in time which gives the normalized transmittance given by the following [40]

$$T = \frac{1}{\sqrt{\pi}q_0} \int_{-\infty}^{\infty} \ln[1 + q_0 e^{-\tau^2}] d\tau, \quad (5.6)$$

where  $q_0$  is defined as

$$q_0 = \beta_2 I_0 (1 - R) L_{eff}, \quad (5.7)$$

where  $I_0$  is the peak incident intensity,  $R$  is the loss due to Fresnel reflections, and  $L_{eff}$  is given by [41]

$$L_{eff} = \frac{1 - e^{-\alpha L}}{\alpha}, \quad (5.8)$$



where  $L$  is the sample thickness and  $\alpha$  is the linear absorption coefficient. In all of the samples, the majority of the linear losses were due to Fresnel losses, while the losses due linear absorption were insignificant. The data for CdTe was plotted versus the dimensionless quantity  $q_0$  and  $\beta_2$  was changed to fit the data to the theory as seen in Figure 5.4. As shown in this figure, the data fits very well to the nonlinear absorption theory defined by Equations (5.6), (5.7), and (5.8). The lenses were switched to vary the intensities, and the overlap of the data is very consistent throughout the experiment. This gives us confidence that there were no experimental errors and the values for  $\beta_2$  are accurate.

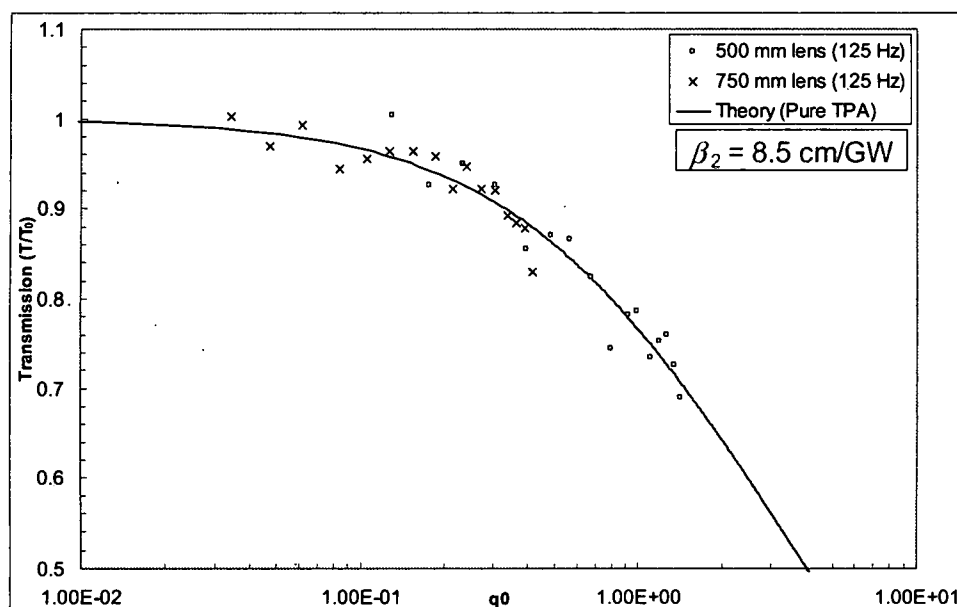


**Figure 5.4 – Nonlinear absorption in a 3 mm sample of CdTe.**

The data collected for the InP semiconductor also has the same consistent data overlap when the lenses were changed and matched the theory well. The data for the InP sample can be seen in Figure 5.5.

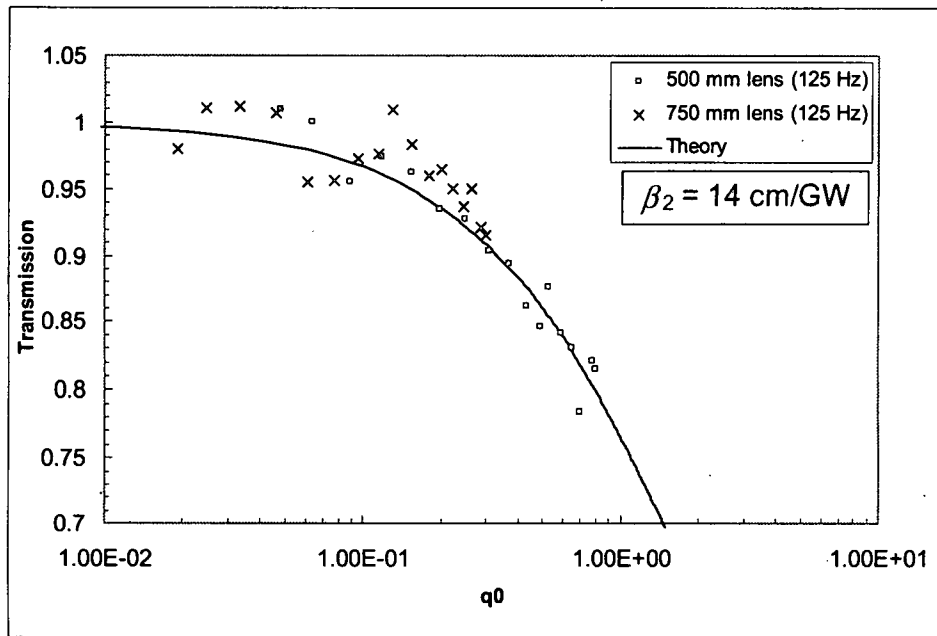


Figure 5.5 – Nonlinear absorption data in a 1.0 mm InP sample.

Silicon being an indirect band-gap material does not have a model to predict the nonlinear absorption coefficient, but it was still measured with good results. From Figure 5.6 it appears that in Si, a purely TPA response exists and follows the theory well for pure TPA given by Equation (5.6). Two samples of different thicknesses of Si were tested, one 5 mm and the other 0.5 mm. The same  $\beta_2$  value was measured for both. The data taken for both Si samples can be seen in Figure 5.6.

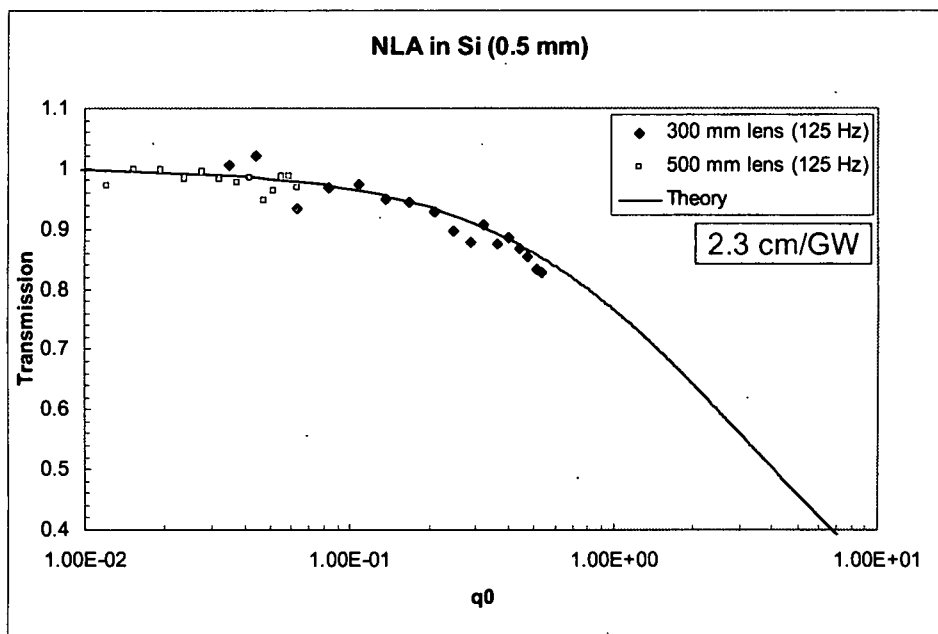
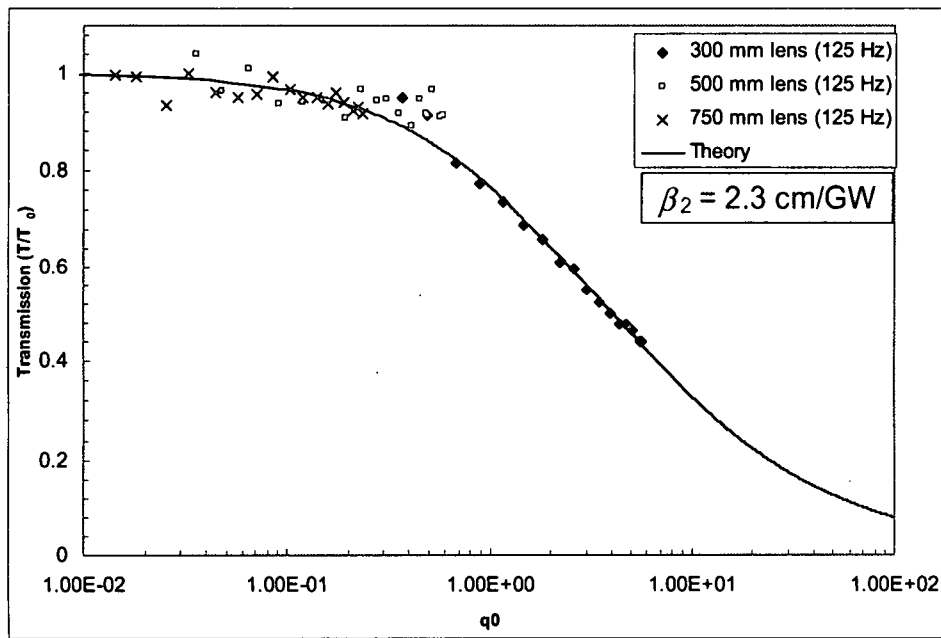


Figure 5.6 – Nonlinear absorption in a 5 mm (top) and 0.5 mm (bottom) sample of Si.

Table 5.1 sums up the  $\beta_2$  measurements made in this experiment along with the theoretical predictions. Notice that all the material band-gaps for each sample tested fell between the incident photon energy and two times the incident photon energy, satisfying

the condition for TPA. Also, the measured  $\beta_2$  values for the direct band-gap materials agreed with the theoretical predictions calculated using Equation (5.5) to within 10% [41].

**Table 5.1 – Theoretical and experimentally measured nonlinear absorption coefficients in three bulk semiconductors.**

$\lambda_p = 1550 \text{ nm}$		$\hbar\omega = 0.8 \text{ eV}$		$2\hbar\omega = 1.6 \text{ eV}$	
Sample	Band-gap (eV)	Gap Nature	Index ( $\lambda$ )	$\beta_2$ theor. (cm/GW)	$\beta_2$ meas. (cm/GW)
Si	1.12 [44]	Indirect	3.52 [45]	N/A	2.3
CdTe	1.44 [42]	Direct	2.74 [46]	8.8	8.5
InP	1.35 [44]	Direct	3.15 [47]	12.4	14

### 5.3 Spectral Broadening in IR materials

The samples were subjected to intense focused laser light to determine if any spectral broadening could be observed at 1550 nm. A 10x microscope objective was used to focus the light from the OPA into the samples. To setup the experiment, a 2 mm sample of B270 was placed at focus from the 10x objective to see if supercontinuum could be generated at 1550 nm and indeed it was generated. The B270 sample was replaced with the three semiconductors: CdTe, InP and Si to determine if any continuum could be observed. When the samples were placed in the focus, they absorbed or limited all of the incident light. There was no detectable signal transmitted through the sample. This observation agrees with the previous studies that supercontinuum can only exist when the incident photon energy is four times larger than the materials band-gap [18]. Since there were no signs of any spectral broadening, and the previous mechanisms from Chapter 4 did not contribute.

## CHAPTER 6

### Conclusions

The nonlinear effects of optical parametric amplification, white-light continuum generation, and two-photon absorption were studied in this thesis. An optical parametric amplifier was refurbished and characterized, and the theory of the nonlinear processes involved was explained. Various transparent glasses were tested to determine the white-light spectral properties in these samples under various focusing conditions. A (1+1) dimensional model was generated which displayed the blue pedestal and off axis conical emission seen in the experimental results. Finally the nonlinear absorption coefficients in three bulk semiconductors were measured and have shown to agree well with theoretical predictions. The OPA was used as the laser source in this experiment.

The OPA was initially completely mis-aligned and many of the optical elements in the device were damaged. Once the OPA was re-aligned and the damaged optical elements were replaced, it was finally able to operate. The optical elements within the device are still susceptible to damage, but with the proper knowledge of the system damage can be easily avoided. The nonlinear optics theory that drives the OPA, difference frequency generation, was covered completely as well as phase matching. The phase matching conditions in the BBO crystals inside the OPA are now known as well as a complete understanding of the nonlinear crystals capabilities. The OPA was

characterized and found to be a tunable femtosecond source from 450 to 2400 nm with micro-joule output energies.

White-light continuum is also a source for femtosecond laser pulses of a variety of colors, but white-light continua gives the entire spectrum at once. This has been a very active area of research in the past five decades, and only now are we beginning to understand all of the nonlinear mechanisms involved in this complicated process. In this work, ten glass samples were tested to determine their white-light spectral properties. Any sample with a band-gap above 4.4 eV exhibited a blue pedestal extending out to at least 420 nm. The flint glass samples whose band-gap were below 3.9 eV, did exhibit some spectral broadening, but did not have the blue pedestal associated with continuum generation in the crown glasses and ionic crystals. The focusing conditions were also changed to determine the spectral response. The experimental data showed that the lower the  $f/\#$  the higher the threshold is for spectral broadening. Also, when the sample thickness was changed the overall continuum generated was not as strong for thinner samples. These results can be attributed to a dependence of the active nonlinear volume in the medium. When a low  $f/\#$  system was used, the active volume was smaller inside the medium which increased the broadening threshold as well as decreased the continuum generated. Continuum generation was not only observed in the forward direction, but it propagates backwards as well. This effect can be attributed to mechanisms that are still unknown since few observations have been made about backward supercontinuum.

A model was developed to simulate SCG in a nonlinear medium. The model was a (1+1) dimensional model which included the following mechanisms: dispersion, space-time focusing, diffraction, self-steepening, self-focusing, self-phase modulation, Kerr

effect, and multi-photon absorption. This model was able to simulate the blue pedestal seen in the white-light experimental data as well as the off axis conical emission. The model, however, is only one-dimensional in space so many of the propagation effects cannot be related to physical data. If radial symmetry was added to the model, it would predict the beam propagation in a more accurate way. This should be taken as a preliminary model which could be the foundation for a more complete simulation later on. This model however does show the same results seen in the experimental data, and is a good tool to complete the understanding of the mechanisms involved in nonlinear pulse propagation and SCG.

The final nonlinear optical research done was with semiconductors. The OPA was used as the laser source for this experiment; it provided femtosecond laser pulses at 1550 nm, an important telecommunications wavelength. Two of the samples, CdTe and InP, were direct band-gap materials whose nonlinear absorption coefficient could be predicted using the two-band model theorized by Van Stryland *et al.* These two coefficients were found to be within good agreement with the model as well as previous measured values. The silicon sample tested had an indirect band structure, so the model could not predict the nonlinear absorption coefficient for this type of material. The nonlinear absorption coefficients were measured and predicted within 10 percent of one another for CdTe and InP. Since the direct band-gap materials were in good agreement with the verified model the nonlinear absorption value obtained for silicon was measured with confidence. The measurements made here were done at 1550, in future measurements, it would be interesting to change the photon energy such that the two-photon energy is varied with respect to the material's band-gap.

## Appendix A

### Supercontinuum Model

```
% Paul Noffke - University of Dayton - WPAFB, OH - April 2006
%
% Fs pulse propagation program including effects from dispersion
% diffraction, space-time focusing, Kerr effect, self-steepening, and
% multi-photon absorption (MPA)
%
% Input data and NLSE from: A. Gaeta, Phys. Rev. Lett. 84, 3582 (2000).
%
% The model simulated SCG under three focusing conditions from a 2.89 mm
% spot size (e-1 radius) using lenses of focal length 20, 10 and 5 cm.
% This preliminary model successfully shows the blue pedestal and off
% axis conical emission.

clear;
tic;                                % Initiate program timer

c=3e10;                             % Speed of light [cm/s]
Pcr=1.8;                             % Critical Power [MW]
P=.6e-12/1.9e-13;                   % Input peak power [MW]
lambda=8e-5;                         % Laser wavelength [cm]
k0=2*pi/lambda;                     % Wave number [cm^-1]
tau_p=1.5e-13;                       % Pulse width [s]
beta_2=1280 ;                       % Sapphire dispersion [fs^2/cm]
Lds=tau_p^2*1e30/beta_2;             % Dispersion length [cm]
r_l=.289;                           % Beam radius into the lens [cm]
f=20;                               % Focal length [cm]
%r_spot=.313e-2;                     % Spot size at focus of 20 cm lens [cm]
%r_spot=.248e-2;                     % Spot size at focus of 10 cm lens [cm]
r_spot=.205e-2;                     % Spot size at focus of 5 cm lens [cm]
Ldf=r_spot^2/2*k0;                   % Diffraction length [cm]
LL=-.15/Ldf;                         % Length from the sample center to sample face
Lnl=Ldf/.948/P/Pcr;                  % Nonlinear length [cm]
Lpl=Ldf*100;                         % Plasma length [cm]
Lmp=Ldf*100;                         % Multi-photon absorption length [cm]
omegataup=100;                      % Self-steepening parameter
omegatauc=5;                        % Plasma coupling parameter
alpha=.1;                           % Avalanche ionization coefficient
alphaMP=1e-6;                       % Multi-photon absorption amplitude
m=5;                                % Multi-photon absorption exponent

D=.3/Ldf;                           % Distance propagated in the sample
```



```

% Higher order dispersion and nonlinear terms in the NLSE
betal=0; % Dispersion (turned off)
beta2=1/omegataup; % Space time term and self-steepening term
sigma_R=.0; % Real Raman contribution (turned off)
real_R=.0; % Imaginary Raman contribution (turned off)
eta0=sqrt(P/Pcr); % Initial Gaussian amplitude

% Define number of time & space points, time & space windows, & step size
n=512; % Number of time points
T0=14; % Time window
dz=1e-3 ; % Step size
nx=512; % Number of fft points in space
X0=20; % Space window

% Define time & wave number vectors
t=0:1/n:1-1/n; % Time vector
k=2*pi*(0:n-1); % Time wave vector
k=[k(1:(n/2+1)) -k(n/2:-1:2)]; % Shift of wave vector
k=k/T0; % Time vector scaled to window size
v=k.*k; % wave vector squared

% Convert frequencies into physical units
f_0=c/lambda; % Center frequency [s^-1]
f_u=k/2/pi/tau_p; % Unscaled frequencies [s^-1]
f_p=f_0+f_u; % Physical frequencies [s^-1]
lambda_p=(c./f_p)*1e7; % Physical wavelengths [nm]

% Define transverse spatial & wave vectors
x=0:1/nx:1-1/nx; % Space vector
q=2*pi*(0:nx-1); % Space wavenumber vector
q=[q(1:(nx/2+1)) -q(nx/2:-1:2)]; % Shift of waven vector
q=q/X0; % Space vector scaled to window size
q2=q.*q; % wave vector squared
angle=q/r_spot/k0*180/pi; % Physical angles [degrees]

dt=1/n*T0; % Time interval
Ainit=zeros(n,nx); % Initialize array for Gaussian beam
rho=zeros(n,nx); % Initialize array for rho
rhop=zeros(n,nx); % Initialize array for rhop

% Define operator for linear diffraction and dispersion part of propagation
for it=1:n;
    for ix=1:nx;
        % propagator for the nonlinear medium
        U(it,ix)=exp(((i*v(it)/2)*(Ldf/Lds + ... % Dispersion
            k(it)*2*betal)... % 3rd order Disp. (off)
            -i*.25/(1 + ... % Diffraction
            k(it)*beta2)*q2(ix))*dz); % Space-time Focusing
        % Free space propagator from the center to the sample surface
        Ufront(it,ix)=exp((-i*.25*q2(ix))*LL);
        % Initial Gaussian beam
        Ainit(it,ix)=eta0*exp(-(T0*(t(it)-0.5)).^2/2-(X0*(x(ix)-0.5)).^2/2);
    end;
end;
end;

```

```

steps=fix(D/dz);           % Number of steps through the sample

ainit=fft2(Ainit);         % Initial intensity spectrum
A=Ainit;                   % Initial Gaussian
Al=A;                      % Initial Gaussian

knt=0;                     % Frequency step
a=fft2(Al);
Al=ifft2(a.*Ufront); % field at the front of the sample
% Define nonlinear operator following the Fourier step method and
% propagate the pulse through the different slices. Start nonlinear
% propagation using finite difference method
for j=1:steps;
    DQ=(A(2,:)-A(1,:))/dt; % DQ=dE/dt
    DSA=(abs(A(2,:)).^2-abs(A(1,:)).^2)/dt; % DSA=d|E|^2/dt
    % NLPert includes the self-steepening (beta2) contributions to the
    % nonlinearity terms of Kerr and mulit-photon absorption
    NLPert=-i*beta2*Ldf/Lnl*DQ.*conj(A(1,:))-... % Kerr
            i*DSA.*(beta2*Ldf/Lnl)... % Kerr
            -beta2*Ldf/Lmp*(abs(A(1,:)).^(2*(m-2))).*((m-1)*DSA+DQ); % MPA
    % Nonlinear propagator through the nonlinear medium
    Al(1,:)=A(1,:).*exp(dz*(i*Ldf/Lnl*abs(A(1,:)).^2+... % Kerr
        NLPert+... % Above term
        i*DSA.*(real_R+i*sigma_R)-... % Raman (off)
        i*Ldf/Lpl*(1-i/omegatauc)*rho(1,:)-... % Plasma Coupling
        alphaMP*abs(A(1,:)).^(2*(m-1)))); % MPA
    % Define rho which includes avalanche ionization an MPA
    rho(2,:)=rho(1,:)+(alpha*rho(1,:).*abs(Al(1,:)).^2+... % Avalanche
        abs(Al(1,:)).^(2*m))*dt; % MPA
    DQ=(A(3,:)-A(2,:))/dt; % DQ=dE/dt
    DSA=(abs(A(3,:)).^2-abs(A(2,:)).^2)/dt; % DSA=d|E|^2/dt
    NLPert=-i*beta2*Ldf/Lnl*DQ.*conj(A(2,:))-... % Kerr
            i*DSA.*(beta2*Ldf/Lnl)... % Kerr
            -beta2*Ldf/Lmp*(abs(A(2,:)).^(2*(m-2))).*((m-1)*DSA+DQ); %MPA
    Al(2,:)=A(2,:).*exp(dz*(i*Ldf/Lnl*abs(A(2,:)).^2+... % Kerr
        NLPert+... % Above term
        i*DSA.*(real_R+ i*sigma_R)-... % Raman (off)
        i*Ldf/Lpl*(1-i/omegatauc)*rho(2,:)-... % Plasma Coupling
        alphaMP*abs(A(2,:)).^(2*(m-1)))); % MPA
    % Predictor Corrector Method to solve for rho
    for it=3:n;
        DQ=(A(it,:)-A(it-1,:))/dt;
        DSA=(abs(A(it,:)).^2-abs(A(it-1,:)).^2)/dt;
        NLPert=-i*beta2*Ldf/Lnl*DQ.*conj(A(it,:))-... % Kerr
                i*DSA.*(beta2*Ldf/Lnl)... % Kerr
                -beta2*Ldf/Lmp*(abs(A(it,:)).^(2*(m-2))).*((m-1)*DSA+DQ); % MPA
        Al(it,:)=A(it,:).*exp(dz*(i*Ldf/Lnl*abs(A(it,:)).^2+...% Kerr
            NLPert+... % Above term
            i*DSA.*(real_R+ i*sigma_R)-... % Raman (off)
            i*Ldf/Lpl*(1-i/omegatauc)*rho(it,:)-... % Plasma
            alphaMP*abs(A(it,:)).^(2*(m-1)))); % MPA
    % Initialize rho
    F=(alpha*rho(it-1,:).*abs(Al(it-1,:)).^2+abs(Al(it-1,:)).^(2*m));
    rho(it,:)=rho(it-1,:)+F*dt; % Predictor step
    Fp=(alpha*rho(it,:).*abs(Al(it,:)).^2+abs(Al(it,:)).^(2*m));

```

```

        rho(it,:)=rho(it-2,:)+(F+Fp)*dt;    % Corrector step
    end;
    % Propagate in the linear regime
    a=fft2(A1); A=ifft2(a.*U);
    knt=knt+1;
    % Maximum of the intensity
    P(knt)=max(max(abs(A).^2)); % Peak Power
    Z(knt)=dz*knt;             % Scaled propagation distance

end;

E=sum(sum(abs(A).^2))*T0/n*X0/nx; % Conservation of the energy check

a2=abs(a).^2;
a2max=max(max(a2));
% Generate the plots
T=t*T0-T0/2;
X=x*X0-X0/2;

% Final intensity plot
figure(1);
[XX,YY]=meshgrid(X,T);
contour(XX,YY,abs(A).^2);
xlabel('x');
ylabel('t');
title('Final Intensity');

% Initial intensity plot
figure(2);
[XX,YY]=meshgrid(X,T);
contour(XX,YY,abs(Ainit).^2);
xlabel('x');
ylabel('t');
title('Initial Intensity');

% Final intensity spectrum plot
figure(3);
[XX,YY]=meshgrid(angle,lambda_p);
contour(XX,YY,abs(a).^2/a2max);
xlabel('Wavelength (nm)');
ylabel('\theta (degrees)');
title('Final intensity spectrum');

% Initial intensity spectrum plot
figure(4);
[XX,YY]=meshgrid(angle,lambda_p);
contour(XX,YY,abs(ainit).^2);
xlabel('\theta (radians)');
ylabel('wavelength (nm)');
title('Initial intensity spectrum');

% Electron density plot
figure(5);
%[XX,YY]=meshgrid(X,T);
%mesh(XX,YY,rho)

```

```

xlabel('x');
ylabel('t');

% Peak power as a function of distance though the sample
figure(6);plot(Z,P);
xlabel('z');
ylabel('Peak Power');

% Final power spectrum (log scale)
aa=sum(abs(a').^2);
aamax=max(aa);
figure(7);plot(lambda_p,log10(aa/aamax));
xlabel('wavelength (nm)');
ylabel('Log(Power Spectrum)');

% Final power spectrum
figure(8);plot(lambda_p,aa/aamax);
xlabel('Wavelength (nm)');
ylabel('Power Spectrum');
toc;           % End Program Timer

```

## REFERENCES

- [1] A. Baltuška, M.S. Pshenichnikov, and D.A. Wiersma, *Amplitude and phase characterization of 4.5-fs pulses by frequency-resolved optical gating*, Opt. Lett. **23**, 1474-1476 (1998).
- [2] P.T.C. So, C.Y. Dong, B.R. Masters, K.M. Berland, *Two-photon excitation fluorescence microscopy*, Annu. Rev. Biomed. Eng. **2**, 399-429 (2000).
- [3] Pastirk, J. Dela Cruz, K. Walowicz, V. Lozovoy, and M. Dantus, *Selective two-photon microscopy with shaped femtosecond pulses*, Opt. Exp. **11**, 1695-1701 (2003).
- [4] C. B. Schaffer, A. Brodeur, J. F. Garca, and E. Mazur, *Micromachining bulk glass by use of femtosecond laser pulses with nanojoule energy*, Opt. Lett. **26**, 93-95 (2001).
- [5] M. Will, S. Nolte, B. N. Chichkov, and A. Tünnermann, *Optical Properties of Waveguides Fabricated in Fused Silica by Femtosecond Laser Pulses*, Appl. Opt. **41**, 4360-4364 (2002).
- [6] Kazushige Yokoyama, Carlos Silva, Dong Hee Son, Peter K. Walhout, and Paul F. Barbara, *Detailed Investigation of the Femtosecond Pump-Probe Spectroscopy of the Hydrated Electron*, J. Phys. Chem. A **102**, 6957-6966 (1998).
- [7] M. Lewenstein, Ph. Balcou, M. Yu. Ivanov, Anne L'Huillier, and P. B. Corkum, *Theory of high-harmonic generation by low-frequency laser fields*, Phys. Rev. A **49**, 2117-2132 (1994).
- [8] O. Svelto, *Principles of Lasers* (Plenum Press, New York, 1998).
- [9] J. X. Zhou, W. Hou, K. X. Yang, S. J. Tsai, and R. G. Michel, *Lasers based on optical parametric devices: wavelength tunability empowers laser-based techniques in the UV, visible, and near-IR*, Focal Point **52**, 176-189, (1998).
- [10] R. W. Boyd, *Nonlinear Optics* (Academic Press, San Diego, 1992).
- [11] K. R. Wilson and V. V. Yakovlev, *Ultrafast rainbow: tunable ultrafast pulses from a solid-state kilohertz system*, J. Opt. Soc. Am. B **14**, 444-448 (1997).

- [12] R. Danielius, A. Piskarskas, A. Stabinis, G. P. Banfi, P. Di Tripani, and R. Righini, *Traveling-wave parametric generation of widely tunable, highly coherent femtosecond light pulses*, J. Opt. Soc. Am. B **10**, 2222-2232 (1993).
- [13] V. G. Dmitriev, G. G. Gurzadyan, D. N. Nikogosyan, *Handbook of Nonlinear Optical Crystals* (Springer, New York, 1995).
- [14] V. Krylov, J. Gallus, U. Wild, A. Kalintsev, and A. Rebane, *Femtosecond noncollinear and collinear parametric generation and amplification in BBO crystal*, Appl. Phys. B **70**, 163 (2000).
- [15] M. Born and E. Wolf, *Principles of Optics* (Cambridge University Press, Cambridge, 1999).
- [16] Sandia National Laboratories, *Download page for SNLO software* (2006) <http://www.sandia.gov/imrl/X1118/xtal.htm>
- [17] R. R. Alfano, *The Supercontinuum Laser Source* (Springer-Verlag, New York, 1989).
- [18] A. Brodeur, S. L. Chin, *Ultrafast white-light continuum generation and self-focusing in transparent condensed media*, J. Opt. Soc. Am. B **16**, 637-650 (1999).
- [19] P. B. Corkum and C. Rolland, *Femtosecond Continua Produced in Gases*, IEEE J. Quantum Electron. **25**, 2634-2639 (1989).
- [20] R. R. Alfano and S. L. Shapiro, *Emission in the region 4000 to 7000 Å via four-photon coupling in glass*, Phys. Rev. Lett. **24**, 584-587 (1970).
- [21] A. Saliminia, S. L. Chin, and R. Vallée, *Ultra-broad and coherent white light generation in silica glass by focused femtosecond pulses at 1.5 μm*, Opt. Express **13**, 5731-5738 (2005).
- [22] Labsphere, Inc., *Spectralon Diffuse Reflectance Material Data Sheet* (2006). [http://www.labsphere.com/uploadDocs/Spectralon%20Diffuse%20Reflectance%20Material\\_189.pdf](http://www.labsphere.com/uploadDocs/Spectralon%20Diffuse%20Reflectance%20Material_189.pdf).
- [23] R. L. Sutherland, *Handbook of Nonlinear Optics* (Marcel Dekker, Inc., New York, 2003), second edn.
- [24] W. L. Smith, P. Lui, and N. Bloembergen, *Superbroadening in H<sub>2</sub>O and D<sub>2</sub>O by self-focused picosecond pulses from a YAlG:Nd laser*, Phys. Rev. A **15**, 2396-2403 (1977).
- [25] A. Brodeur and S. L. Chin, *Band-gap dependence of the ultrafast white-light continuum*, Phys. Rev. Lett. **80**, 4406-4409 (1998).

- [26] K. D. Moll, D. Homoelle, A. L. Gaeta, and R. W. Boyd, *Conical harmonic generation in isotropic Materials*, Phys. Rev. Lett. **88**, 153901 (2002).
- [27] D. M. Roessler and W. C. Walker, *Electronic Spectra of Crystalline KCl*, Phys. Rev. **166**, 599-606 (1968).
- [28] R. DeSalvo, A. A. Said, D. J. Hagan, E. W. Van Stryland, M. Sheik-Bahae, *Infrared to ultraviolet measurements of two-photon absorption an  $n_2$  in wide band gap solids*, IEEE J. Quantum Electron. **32**, 1324-1333 (1996).
- [29] Z. A. Weinberg, G. W. Rubloff, E. Bassous, *Transmission, photoconductivity, and the experimental band gap of thermally grown  $\text{SiO}_2$  films*, Phys. Rev. B **19**, 3107-3117 (1979).
- [30] I. Golub, *Optical characteristics of supercontinuum generation*, Opt. Lett. **15**, 305-307 (1990).
- [31] J. Watson, F. Salin, P. Georges, and A. Brun, *Conical emission accompanying spectral continuum generation: a Cerenkov-based effect*, SPIE **2041**, 120-126 (1994).
- [32] S. L. Chin, *The physics and the chanllenge of the propagation of powerful femtosecond laser pulses in optical media*, La Physique au Canada **60**, 273-281 (2004).
- [33] J. B. Achcom, C. B. Scaffer, E. Mazur, *Numerical aperture dependence of damage and white light generation from femtosecond laser pulses in bulk fused silica*, SPIE **4633**, 107-111 (2002).
- [34] J. Yu, D. Mondelain, G. Ange, R. Volk, S. Niedermeier, and J. P. Wolf, *Backward supercontinuum emission from a filament generated by ultrashort laser pulses in air*, Opt. Lett. **26**, 533-535 (2001).
- [35] J. H. Marburger, *Self-focusing: theory*, Prog. Quant. Electron. **4**, 35-110 (1975).
- [36] A. L. Gaeta, *Catastrophic collapse of ultrashort pulses*, Phys. Rev. Lett. **84**, 3582-3585 (2000).
- [37] P. Chernev and V. Petrov, *Self-focusing of light pulses in the presence of normal group-velocity dispersion*, Opt. Lett. **17**, 172-174 (1992).
- [38] J. E. Rothenberg, *Space-time focusing: breakdown of the slowly varying envelope approximation in the self-focusing of femtosecond pulses*, Opt. Lett. **17**, 1340-1342 (1992).

- [39] L. V. Keldysh, *Zh. Eksp. Teor. Fiz.* **47** 1945 (1964) [*Sov. Phys. JETP* **20** 1307 (1965)].
- [40] M. Sheik-Bahae, A. A. Said, T. Wei, D. J. Hagan, and E. W. Van Stryland, *Sensitive measurement of optical nonlinearities using a single beam*, *IEEE Jour. Quant. Electron.* **26**, 760-769 (1990).
- [41] E. W. Van Stryland, M. A. Woodall, H. Vanherzeele, and M. J. Soileau, *Energy band-gap dependence of two-photon absorption*, *Opt. Lett.* **10**, 490-492 (1985).
- [42] T. D. Krauss and F. W. Wise, *Femtosecond measurement of nonlinear absorption and refraction in CdS, ZnSe, and ZnS*, *Appl. Phys. Lett* **65**, 1739-1741 (1994).
- [43] E. W. Van Stryland, H. Vanherzeele, M. A. Woodall, M. J. Soileau, A. L. Smirl, S. Guha, and T. F. Boggess, *Two photon absorption, nonlinear refraction, and optical limiting in semiconductors*, *Opt. Eng.* **24**, 613-623 (1985).
- [44] B. E. A. Saleh, and M. C. Teich, *Fundamentals of Photonics* (John Wiley & Sons, Inc., United State of America, 1991).
- [45] S. Adachi, *Model dielectric constants of Si and Ge*, *Phys. Rev. B* **38**, 12966-12976 (1988).
- [46] D. T. F. Marple, *Refractive index of ZnSe, ZnTe, and CdTe*, *J. Appl. Phys* **35**, 539-542 (1964).
- [47] S. Adachi, *Model dielectric constants of Gap, GaAs, GaSb, InP, InAs, and InSb*, *Phys. Rev. B* **35**, 7454-7463 (1987).



R002588705

**The HF Group**

Indiana Plant

T 052545 F 24 00



6/8/2006